To Appear in the Astrophysical Journal

Hierarchical Formation in Action: Characterizing Accelerated Galaxy Evolution in Compact Groups Using Whole-Sky WISE Data

Catherine Zucker

Department of Astronomy, University of Virginia, Charlottesville, VA, 22904

Harvard-Smithsonian Center for Astrophysics, Cambridge, MA, 02138

Lisa May Walker

Department of Astronomy, University of Arizona, Tucson, AZ, 85721

Kelsey Johnson

Department of Astronomy, University of Virginia, Charlottesville, VA, 22904

Sarah Gallagher

Department of Physics and Astronomy, University of Western Ontario, London, Ontario N6A 3K7 Canada

Centre for Planetary and Space Exploration, University of Western Ontario, London, Ontario N6A 3K7 Canada

Katherine Alatalo

Hubble Fellow, Carnegie Observatories, Pasadena, CA, 91101

Infrared Processing and Analysis Center, California Institute of Technology, Pasadena, California, 91125

Panayiotis Tzanavaris

Laboratory for X-Ray Astrophysics, NASA Goddard Spaceflight Center, Mail Code 662, Greenbelt, MD, 20771, USA

CRESST, University of Maryland Baltimore County, 1000 Hilltop Circle, Baltimore MD 21250 USA

Department of Physics and Astronomy, The Johns Hopkins University, Baltimore, MD 21218, USA

catherine.zucker@cfa.harvard.edu

ABSTRACT

Compact groups provide an environment to study the growth of galaxies amid multiple prolonged interactions. With their dense galaxy concentrations and relatively low velocity dispersions, compact groups mimic the conditions of hierarchical galaxy assembly. Compact group galaxies are known to show a bimodality in *Spitzer* IRAC infrared colorspace: galaxies are preferentially either quiescent with low specific star formation rates, or are prolifically forming stars—galaxies with moderate levels of specific star formation are rare. Previous *Spitzer* IRAC studies identifying this "canyon" have been limited by small number statistics. We utilize whole-sky WISE data to study 163 compact groups, thereby tripling our previous sample and including more galaxies with intermediate mid-IR colors indicative of moderate specific star formation rates (SSFRs). We define a distinct WISE mid-IR color-space ($\log[\frac{f_{12}}{f_{4.6}}]$ vs. $\log[\frac{f_{22}}{f_{3.4}}]$) that we use to identify canyon galaxies from the larger sample. We confirm that compact group galaxies show a bimodal distribution in the mid-infrared and identify 37 canyon galaxies with reliable photometry and intermediate mid-IR colors. Morphologically, we find that the canyon harbors a large population of both Sa-Sbc and E/S0 type galaxies, and that they fall on the optical red sequence rather than the green valley. Finally, we provide a catalog of WISE photometry for 567 of 652 galaxies selected from the sample of 163 compact groups.

Subject headings: galaxies: evolution — galaxies: interactions — galaxies: groups

1. Introduction

With their high number densities, low velocity dispersions, and frequent reservoirs of intragroup diffuse gas (Hickson et al. 1992), compact groups are dense associations of three or more bright galaxies that routinely undergo prolonged gravitational interactions (Hickson et al. 1992). Due to these properties, they bear a strong resemblance to conditions in the earlier universe, making them an ideal laboratory for studying physical processes such as the formation of central supermassive black holes, galaxy clusters, super-star clusters, and dwarf galaxies experiencing multiple interactions (Konstantopoulos et al. 2013; Tzanavaris et al. 2014). Compact groups also play a critical role in understanding galaxy evolution, as their frequent gravitational interactions affect the gas processing and specific star formation rates (SSFR; star formation rate per stellar mass) of member galaxies. They also tend to be more difficult to characterize than either galaxy clusters or merging pairs: unlike virialized galaxy clusters with thousands of members, compact groups may be more sensitive to the initial configuration of the handful group members, and, unlike galaxy pair mergers, initial conditions in compact groups are more difficult to constrain with models due to a large number of free parameters.

In order to assess the impact of the compact group environment on star formation and galaxy evolution, Johnson et al. (2007) studied the mid-infrared colors of these galaxies and discovered an underdensity between compact group galaxies that are actively star-forming and those that are relatively quiescent. The underdensity in colorspace suggests a rapid transformation of galaxy properties, in the sense that this dearth in *Spitzer* IRAC colorspace ($\log[\frac{f_{8.0}}{f_{4.5}}]$ vs. $\log[\frac{f_{5.8}}{f_{3.6}}]$) is a transition region between spirals and bulge-dominated galaxies (Walker et al. 2010). This transition region, or IRAC "canyon", is occupied by relatively few galaxies with moderate SSFRs and not seen in comparison samples of field galaxies, interacting pairs, or the center of the Coma Cluster (Walker et al. 2010, 2012). The Coma infall region is the only comparison sample that shows a similar distribution to compact group galaxies in IRAC colorspace (Walker et al. 2012). This is consistent with the idea that the infall region best mimics the properties of the compact group environment, as they both have high galaxy densities and reservoirs of cold gas. Finally, in addition to showing a bimodality in mid-IR colorspace, Tzanavaris et al. (2010) also find a significant gap between low ($\leq 4.3\times10^{-12}$ yr^{-1}) and high ($\geq 1.6\times10^{-11}$ yr^{-1}) SSFR systems in the compact group environment. The recent work of Lenkic et al. (2016, MNRAS, Submitted) further supports this SSFR bimodality. The lack of compact group galaxies with moderate levels of specific star formation, in contrast to other environments, implies that *compact group galaxies experience accelerated evolution.* Star formation enhancement due to gravitational interactions (including mergers) of galaxies in this dense environment likely also plays a role in this observed bimodality.

To further investigate the nature of compact group galaxies, Cluver et al. (2013) used the *Spitzer* Infrared Spectrograph (IRS) to study the PAH and H_2 lines in the systems. The first compact group studied in detail in this way was Stephan's Quintet (Appleton et al. 2006; Cluver et al. 2010), where enhanced warm H_2 emission was seen in quantities that could not be explained by photoionization from star-forming regions alone. This emission was associated with the large bow-shock seen between the intruder (NGC 7319) and the interacting pair (NGC 7318a & 7318b). Cluver et al. (2013) followed up this effort, investigating the mid-IR spectral properties of 74 galaxies in 23 Hickson Compact Groups, including 17 galaxies within the original IR gap of Johnson et al. (2007). These results show that the galaxies that are in the IR gap are the most likely to show enhanced warm H_2 from *Spitzer*, and thus are considered galaxies most likely to have shock-enhanced interstellar media, hinting that shocks in these systems might be a significant contributor to canyon galaxies' rapid evolution.

All previous IR-based studies — using data from the *Spitzer Space Telescope* – are limited by their small sample sizes. Johnson et al. (2007) studied only 12 compact groups (45 galaxies), while Walker et al. (2012) only studied 49 compact groups (174 galaxies). The largest sample (Walker et al. 2012) yielded only five galaxies located in the mid-infrared canyon region, a minuscule number when one seeks to understand the properties of these unique galaxies and their evolution. The small sample sizes of previous studies are due to both limited sky coverage and the narrow imaging bands of *Spitzer*, which forces a redshift cut as the polycyclic aromatic hydrocarbon (PAH) features shift out of the 8μm band at $z = 0.035$. In contrast, the Wide-field Infrared Survey Explorer (WISE)

telescope has whole-sky coverage and bands wide enough that the PAH features do not shift out of the 12μm band until $z = 0.52$. Using WISE data, we perform analyses similar to those of Johnson et al. (2007) and Walker et al. (2012). We expand the sample selection to a total of 163 compact groups (652 member galaxies), thereby drawing from all 49 groups from Walker et al. (2012), plus an additional 114 groups, increasing the number of compact groups with mid-IR analyses by a factor of three. In doing so, we are able to identify additional galaxies in the mid-infrared canyon region, producing a sizable sample of moderate SSFR galaxies that will enable a more comprehensive analysis of the processes that influence galaxy evolution in this environment.

2. Data

2.1. Sample

For this study, we draw our sample from groups in the Hickson Compact Group catalog (HCG, Hickson 1982) and the Redshift Survey Compact Group catalog (RSCG, Barton et al. 1996). Since our sample is culled from two different catalogs, it is necessary to consider their differing selection criteria. The original 100 Hickson Compact Groups were identified through a systematic visual search of the Palomar Observatory Sky Survey prints. In the original sample, each HCG had to contain at least four galaxies (within three magnitudes of the brightest galaxy) and had to satisfy isolation and compactness criteria—requirements that excluded the addition of galaxy clusters in the catalog. Follow-up radial velocity data indicated that several groups had only three members within 1000 km s^{-1} of the median group velocity, but these groups were not rejected (Hickson et al. 1992). Seven other groups (HCGs 9, 11, 18, 36, 41, 77, 78) were shown to have less than three accordant members, and these groups are excluded from our analysis (Hickson et al. 1992). Following the convention from Hickson et al. (1992), we also exclude discordant galaxies that by projection appear to be members of accordant groups.

In contrast to the HCGs, the 89 RSCGs were chosen from a complete, magnitude-limited redshift survey, using a friends-of-friends algorithm, with parameters chosen to identify compact groups similar to the HCGs (Barton et al. 1996). "Neighbors" were identified based on projected separation ($\Delta d < 50$ kpc) and median radial velocity difference ($\Delta v < 1000$ km s^{-1}). The radial velocity criterion is concordant with Hickson's procedure of rejecting group members with a median line-of sight velocity difference > 1000 km s^{-1} (Hickson et al. 1992). Unlike Hickson, Barton et al. (1996) did not take galaxy magnitudes into account, nor did they implement Hickson's isolation criterion. As a result, some RSCGs are embedded in clusters, with the most extreme examples being RSCGs 67 and 68 (embedded in the Coma Cluster), RSCG21 (embedded in the Perseus Cluster), and RSCG11 (embedded in the core of Abell cluster 194). It is important to recognize that the cluster environment acts as a confounding variable in our analysis of the compact group environment, so we have excluded the most extreme examples—RSCGs 11, 21, 67, and 68—from our analysis. Several other RSCGs are located on the edge of clusters, including RSCG12 on the

outskirts of the Zwicky cluster (Barton et al. 1998), or RSCG65 on the outskirts of the Virgo cluster (Barton et al. 1996). As the cluster outskirt environment is expected to be less of an influence than the cluster core environment (being the only other comparison sample from Walker et al. (2010) to exhibit a gap), we include these groups in our analysis. Finally, though the HCG and RSCG catalogs had different selection criteria, there are fifteen RSCGs that are either HCGs or part of HCGs. In these instances, we only use the HCG group to avoid double-counting. Excluding all discordant HCGs (7 groups) and RSCGs embedded near the core of clusters (4 groups), our final tally of distinct compact groups is 163 (93 HCGs and 70 RSCGs), totaling 652 constituent galaxies.

2.2. WISE Photometry

The original ALLWISE atlas images are intentionally blurred, with their PSF profiles having FWHM values which are $\sqrt{2}$ times larger than the single exposure values. As such, we utilize new ALLWISE coadds[1] from Lang (2014), which preserve the native resolution of the raw frames ($\approx 6.1'', 6.4'', 6.5''$, and $12.0''$ for bands W1, W2, W3, and W4). We convert to Janskys using $f_0 \times 10^{-0.4\mathrm{MAGZP}}$, taken from Section 4.3 in the explanatory supplement for the ALLWISE image atlas. We adopt the same zero magnitude flux densities (f_0 =306.682, 170.663, 29.0448, and 8.2839 for W1, W2, W3, and W4) implemented in the conversion of ALLWISE source catalog raw fluxes to magnitudes, which assumes a f_ν^{-2} power law spectra. The zero-point value MAGZP equals 22.5 for all four bands, as Lang (2014) scale the reprocessed ALLWISE atlas images to this zero point. To ensure a common pixel scale and resolution, we convolve the W1 (3.4μm), W2 (4.6μm), and W3 (12μm) images to the W3 PSF, using the WISE "frame" kernels from Aniano et al. (2011). We avoid convolving to the W4 (22μm) PSF, as this band has low sensitivity and will only add noise for a majority of the galaxies. Instead, we derive an independent aperture for galaxies with high signal-to-noise in W4, and pull the rest of the photometry from the ALLWISE source catalog for unresolved or low signal-to-noise systems.

We perform photometry on the convolved W1, W2, and W3 images and select W4 images using SURPHOT, a multi-wavelength photometry code which measures flux densities within a single aperture across multiple wavebands (Reines et al. 2008). We use SURPHOT to detect a contour level (1-3σ above the background) in a specified region of a reference image—an averaged, weighted (λ^{-1}) image of the W1,W2, and W3 bands (hereafter referred to as W123). As the W123 reference image is weighted by λ^{-1}, W1 drives the aperture, followed by W2 and W3. Once an aperture is determined using the reference image, SURPHOT assigns this reference aperture identically to the first three WISE bands. Three sets of background annuli are also applied by expanding the aperture in W123 by two specified factors ($2.0-2.5\times, 2.0-3.0\times, 2.5-3.0\times$), which are then applied to the W1, W2, and W3 bands. For each annulus ($2.0-2.5\times, 2.0-3.0\times, 2.5-3.0\times$), the background flux is calculated using both the mode and the resistant mean, which reduces the effect

[1] http://unwise.me/

of neighboring galaxies contaminating the background annulus. These local background fluxes are then subtracted from the source flux. Uncertainties are calculated for all SURPHOT fluxes by determining the standard deviation in the set of fluxes due to differences in the background. As the background flux is calculated in six ways (mode and the resistant mean for the three types of background annuli), we determine the standard deviation in the set of six background-subtracted source fluxes.

Thus, we divide the photometry into three groups, based on their resolution and signal-to-noise ratio in W1 through W4:

1. For galaxies resolved in W1, W2, W3, and W4, we perform photometry on W1, W2, and W3 with SURPHOT, applying a matched aperture derived from W123 to each of the first three convolved images. We then use SURPHOT to define an independent aperture using only the W4 image. To determine whether a source is resolved in W4, we use the reduced χ^2 of the W4 profile-fit photometry measurement ("w4rchi2") from the ALLWISE source catalog. This parameter indicates the goodness of fit between the source and the PSF, with resolved and extended galaxies exhibiting larger χ^2. We flag any galaxy with w4rchi2 > 2 as a resolved and extended source. Of the 652 galaxies in our sample, 59 galaxies are individually resolved in the W123 reference image and also have w4rchi2 ≥ 2, so SURPHOT is used to calculate fluxes in all four bands.

2. For galaxies resolved in W1, W2, and W3, but with a w4rchi2 < 2, we perform photometry on W1, W2, and W3 using the same methodology as above and pull the W4 fluxes (w4mpro) from the ALLWISE source catalog.

3. For galaxies that a) have too low signal-to-noise for us to apply a 1σ contour to them and b) cannot be individually resolved with a 3σ contour due to small projected separation, we pull photometry for W1, W2, W3, and W4 (w1mpro,w2mpro,w3mpro,w4mpro) from the ALLWISE source catalog

Star subtraction is done on all SURPHOT galaxies where a confirmed star is visible within the galaxy aperture (15 galaxies). We use the stellar-dominated band with the larger PSF (W2) to define a circular aperture around the star, and this is then subtracted from the W1 through W3 fluxes. No star-subtracted galaxies are resolved in W4, so the W4 fluxes for these 15 galaxies are pulled from the ALLWISE catalog.

As the WISE absolute photometric calibration is based on profile-fitting of point sources, we also apply a flux correction to account for the extended nature of our galaxies. Jarrett et al. (2013) gives the corrections in magnitudes: $+0.034, +0.041, -0.030, +0.029$, for the 3.4μm, 4.6μm, 12μm, 22μm bands, respectively. We convert from a magnitude correction to a flux correction using the relationship $m_{apcor} = -2.5 \log_{10} f_{apcor}$, taken from section 2.3 of the WISE preliminary explanatory supplement.

Though most groups are local, there are several with redshifts exceeding 0.1. For the sake of consistency, we apply a k-correction to all galaxies using the low resolution spectral templates and FORTRAN fitting code from Assef et al. (2010). Assef et al. (2010) determine low resolution empirical SED templates from the near-ultraviolet (0.03 μm) to the mid-infrared (30 μm) that accurately reproduce galaxy properties. Their methodology is based upon the assumption that every galaxy SED is some linear combination of old stellar populations, continuously star-forming populations, starbursting populations, and post-starbursting populations. We apply the Assef et al. (2010) fitting routine to our WISE W1 through W4 fluxes, using the spectral response curves from Wright et al. (2010). We note that for a small subset of the sample ($\approx 15\%$ of the full sample) the fitting routine returns a high reduced χ^2_ν value ($\chi^2_\nu > 150$); this occurs preferentially for galaxies with high signal-to-noise in W4, to which we independently fit an aperture using SURPHOT. None of the galaxies with poor χ^2_ν values are in high redshift groups, and we expect this effect to be negligible. A majority of the galaxies in our full sample yield a $\chi^2_\nu \lesssim 1$.

Finally, 77 of the 652 galaxies are either not identified in the ALLWISE source catalog (to within $5''$) or have a negative flux measurement provided by the catalog, so these galaxies are excluded from the sample. We also impose a signal-to-noise cutoff of 2 in all four bands, as the WISE profile-fit magnitude is substituted with a 2σ brightness upper limit when the source fails to meet this signal-to-noise cutoff. Providing that the galaxy has an upper limit in only a single band, we include galaxies with $0 < S/N < 2$, but mark them as such in all color-color plots. Our final sample of galaxies, including those with upper limits in one band, is 567 galaxies (428 with reliable photometry and 139 with upper limits).

2.3. SDSS Photometry

In §3.5, we plot the distribution of a subsample of our galaxies in SDSS colorspace, and we derive our u, g, r, i photometry for this analysis from the DR12 SDSS photometric catalog.[2] We use model magnitudes ("modelMag"), which implement the better of two fits (de Vaucouleurs and exponential model) in the r-band to derive a matched aperture and determine the flux through all bands; modelMags are recommended for calculating the colors of extended objects.[3]. We apply standard Galactic extinction corrections in magnitudes following Schlegel et al. (1998). While we use the Assef et al. (2010) code to correct the mid-infrared fluxes, we k-correct our SDSS magnitudes using the IDL routine calc_kcor.pro from Chilingarian & Zolotukhin (2012).

[2]http://skyserver.sdss.org/dr12/en/tools/crossid/crossid.aspx

[3]https://www.sdss3.org/dr10/algorithms/magnitudes.php#mag_model

3. Results and Discussion

3.1. Comparison of IRAC and WISE Colorspaces

Since the available WISE bands [3.4μm (W1), 4.6μm (W2), 12μm (W3), 22μm (W4)] are different from the Spitzer IRAC bands [3.6μm (IRAC1), 4.5μm (IRAC2), 5.8μm (IRAC3), 8.0μm (IRAC4)], we can not directly map *Spitzer* IRAC colors to WISE colors. In creating a distinct region of WISE color-color space, we need to be cognizant of the similarities and differences between the two instruments. As shown in Jarrett et al. (2011), the passbands for W1 and W2 closely correspond to the passbands for IRAC1 and IRAC2, though W1 tends to be slightly bluer with respect to IRAC1, while W2 is slightly redder with respect to IRAC2 (see Figure 1 from Jarrett et al. 2011), though this should have minimal impact on our results. Moreover, W3 has almost no overlap with IRAC4, and the W3 band should be more sensitive to 11.3μm PAH emission and 10μm silicate absorption in nearby star-forming galaxies, though it will be less sensitive to the stronger PAH features at 6.2μm and 7.7μm (Jarrett et al. 2011). Thus, a) both W1 and W2 and IRAC1 and IRAC2 are dominated by stellar photospheric emission while b) W3 will be more sensitive than IRAC4 to 11.3μm PAH emission in nearby galaxies and c) W4 has no IRAC comparison band (it is closest to the 24μm band on MIPS), and will have large contributions from relatively warm thermal dust emission, if present.

Since different mid-infrared bands are probes of different emission mechanisms, we can use different color combinations to separate galaxies that are actively star forming from those that are relatively quiescent. Using IRAC colors, Walker et al. (2012) are able to separate galaxies dominated by stellar light from galaxies dominated by PAH and thermal dust emission, by plotting $\log[\frac{f_{8.0}}{f_{4.5}}]$ vs. $\log[\frac{f_{5.8}}{f_{3.6}}]$. This is shown in the left panel of Figure 1. For the 141 galaxies in our full sample that we have in common with the sample of Walker et al. (2012), we are able to reproduce this same trend by plotting $\log[\frac{f_{12}}{f_{4.6}}]$ vs. $\log[\frac{f_{22}}{f_{3.4}}]$, as shown in the right panel of Figure 1. Unfortunately, the two bounding canyon galaxies from the Walker et al. (2012) sample (HCG37e & HCG57h) have a low signal-to-noise in the 22μm band, so we are not able to directly map the IRAC canyon to the WISE canyon. Instead, we use the full sample to statistically define the bimodality in §3.2.

Comparing the two distributions, it appears that the spread of galaxies in WISE colorspace shows more scatter than their spread in IRAC colorspace. We attribute this in part to larger photometric errors induced by the introduction of the lower resolution and lower sensitivity WISE 22μm and 12μm bands and the smaller aperture of the WISE instrument. In addition to larger photometric errors, we hypothesize that the WISE canyon could potentially be less prominent than the *Spitzer* canyon due in part to the inclusion of these higher wavelength bands, which probe a different regime than the $3-8\mu$m IRAC bands. It is generally assumed that $6-9\mu$m features (traced by IRAC4), will be stronger in ionized PAHs (PAH^+), while the 11.3μm feature (traced by W3) will be stronger in neutral PAHs (PAH^0) (Galliano et al. 2008; Wu et al. 2010; Sadjadi et al. 2015). As such, the UV-excited 7.7μm feature preferentially traces current star formation, while the 11.3μm feature preferentially traces the diffuse ISM, and is often found in early-type galaxies

with low star formation rates (see Cluver et al. (2013) and references therein). Moreover, there is no IRAC comparison band for W4, which traces relatively warm thermal dust emission.

Along this line of thought, Alatalo et al. (2014) show an "elbow" between late and early type galaxies in WISE [W1-W2] vs. [W2-W3] colorspace and hypothesize that this result is due to the fact that galaxies transition in optical colors (quenching star formation) before IR color (shedding their interstellar media, as traced by the thermal dust 22μm emission and 11.3μm neutral PAH feature), a finding also suggested in Walker et al. (2013). If the WISE canyon seen in compact groups is also caused in part by the shedding of the galaxies' ISM, this could explain why the canyon is less prominent in WISE colorspace than in *Spitzer* color space. Since no IRAC bands adequately trace the 22μm thermal dust emission or the 11.3 micron neutral PAH emission, ISM levels would not significantly contaminate the distribution of galaxies, potentially producing a cleaner spread in IRAC colorspace.

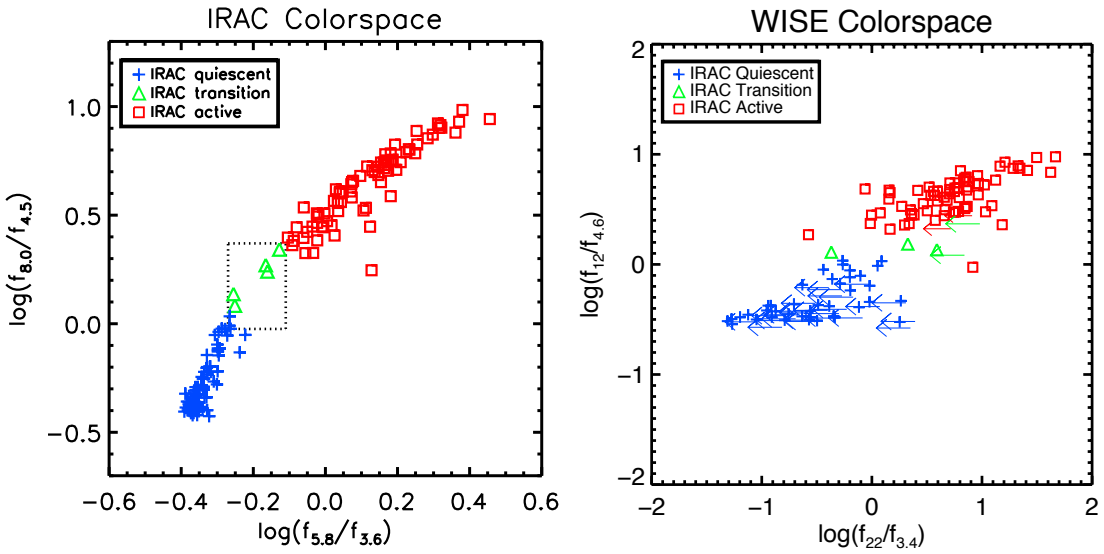

Fig. 1.— *Left:* IRAC colorspace distribution of the sample of 174 galaxies from Walker et al. (2012). *Right:* WISE colorspace distribution of all the galaxies common to both the Walker et al. (2012) sample and our full sample (141 galaxies). The galaxies in WISE colorspace are color-coded by their location in IRAC colorspace.

3.2. WISE Colorspace Distribution for Full Sample

Having demonstrated the bimodality of the Walker et al. (2012) *Spitzer* sample in WISE color-color space, we plot the distribution of our final sample in Figure 2. Though less pronounced than in Walker et al. (2012) and Johnson et al. (2007), there is still a visible underdensity of galaxies apparent in both samples. We note that galaxies with low signal-to-noise in W4 potentially contaminate the WISE canyon at low $\log[\frac{f_{12}}{f_{4.6}}]$ color, and that these galaxies would likely shift

leftward towards the quiescent population with more reliable photometry. This leftward shift would then further demarcate the canyon region, producing a greater resemblance to the bimodality in Walker et al. (2012). We emphasize that W4 only achieves a 5σ point source sensitivity of ≈ 6 mJy, so this is expected to have a tangible effect on those systems with minimal emission at 22μm.

To define the location of the WISE canyon, we fit isodensity contours to the full sample. We determine the two-dimensional density function of the $\log[\frac{f_{12}}{f_{4.6}}]$ and $\log[\frac{f_{22}}{f_{3.4}}]$ colors using the IDL routine hist_2d.pro, adopting a bin size of 0.3 x 0.3. To provide some smoothing, we interpolate the image to a grid 5× smaller by using the IDL routine min_curve_surf.pro. Assuming Poisson statistics, we determine the minimum contour level that separates the active and quiescent populations (n=12.85 galaxies per bin). We then define the bulk of the active and quiescent populations as regions lying at least 2σ above this density threshold. With a Poissonian distribution, $\sigma = \sqrt{\mu}$=3.58 galaxies per bin, so the 2σ contours above our minimum threshold lie at n=20.01 galaxies per bin. We determine a line-of-best fit for the full sample, and then draw lines perpendicular to this fit and intersecting the 2σ contours at the points where the distance between the two contours is at a minimum. The region bounded by these two perpendicular lines becomes our WISE canyon.

In Figure 2 we overlay the contours which lie $\pm 2\sigma$ (n=5.69, and n=20.01 galaxies per bin) from the minimum contour level separating our active and quiescent regions (n=12.85 galaxies per bin). We plot the line-of-best fit using the dotted line and the canyon boundaries with the perpendicular dashed lines. Using this canyon definition, we color-code the galaxies as either "quiescent", "canyon", or "active". Of the 567 galaxies in our full sample, 57 (10%) fall in the WISE canyon compared to only 5 galaxies (3%) from the Walker et al. (2012) "rotated" sample. *We emphasize that a significant fraction (20 of 57) canyon galaxies have unreliable photometry in W4, and would likely become "quiescent" with more reliable data, so we focus much of our analysis on the 37 canyon galaxies with high signal-to-noise in all four bands.* A list of results and properties for all galaxies in our full sample is shown in the Appendix.

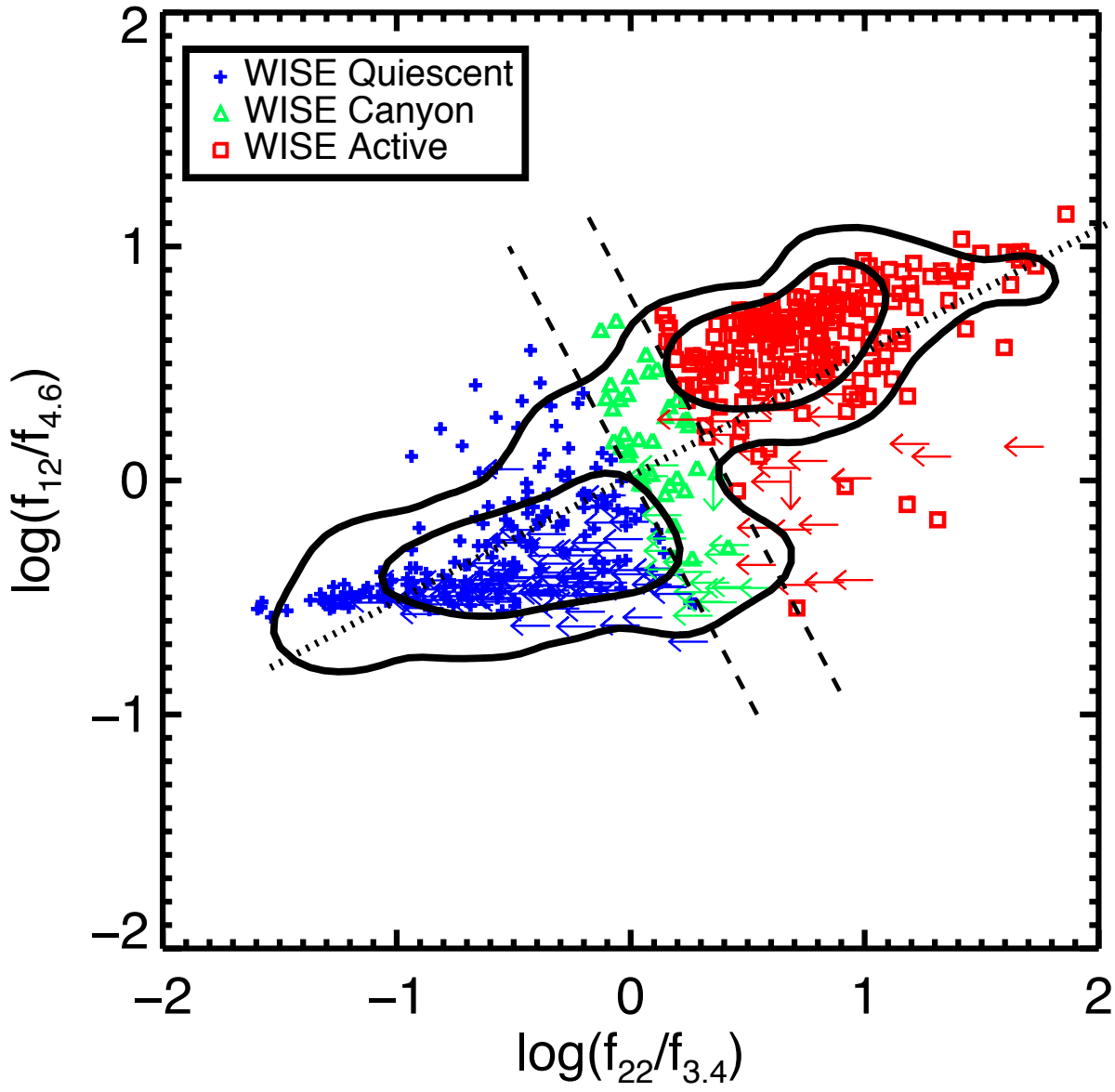

Fig. 2.— WISE colorspace distribution of our full sample. We overlay isodensity contours ($n = 5.69, 20.01$ galaxies per bin) on to our full sample, along with a line-of-best fit (dotted line) and the canyon bounds (dashed lines). We color-code galaxies by their location in WISE color-color space. We fit a canyon to the full sample by a) determining the minimum contour level that separates the active and quiescent populations and b) defining these regions as those lying at least 2σ above this density threshold. We determine a line-of-best fit for the full sample, and then draw lines perpendicular to this fit and intersecting the 2σ contours at the points where the distance between the two contours is at a minimum.

Walker et al. (2012) consider the mid-IR colors of their sample in two ways: rotated so that a straight line fit to the colorspace distribution (left panel of Figure 1) becomes the axis, and unwrapped so that a curve fit to the colorspace distribution becomes the axis. In both cases, the sample is shifted to a mean value of zero. As seen in the top panel of Figure 3, they define the canyon to be where the histogram is less than half its median value; the difference in the canyon bounds produced by the two methods was not statistically significant. For this work, we consider only the rotated distribution, as our WISE colorspace distribution lacks the curvature of the IRAC distribution. Figure 3 shows the rotated mid-IR colors for the Walker et al. (2012) sample (top panel) alongside our full sample (bottom panel); we mark the boundaries of the canyon in both samples with the vertical dotted lines. We see that our WISE canyon, applied in two-dimensions, agrees fairly well with the underdensity apparent in the one-dimensional distribution. This underdensity could potentially become more pronounced with more reliable photometry, as the upper limit canyon galaxies, most of which lie in the C_{MIR_WISE} bin centered at -0.05, would shift towards more negative C_{MIR_WISE} values. We also see that, although both IRAC and WISE show a bimodal distribution, our WISE sample is broadened in C_{MIR_WISE} when compared to IRAC, which makes sense given that WISE probes a much broader range of ISM parameter space.

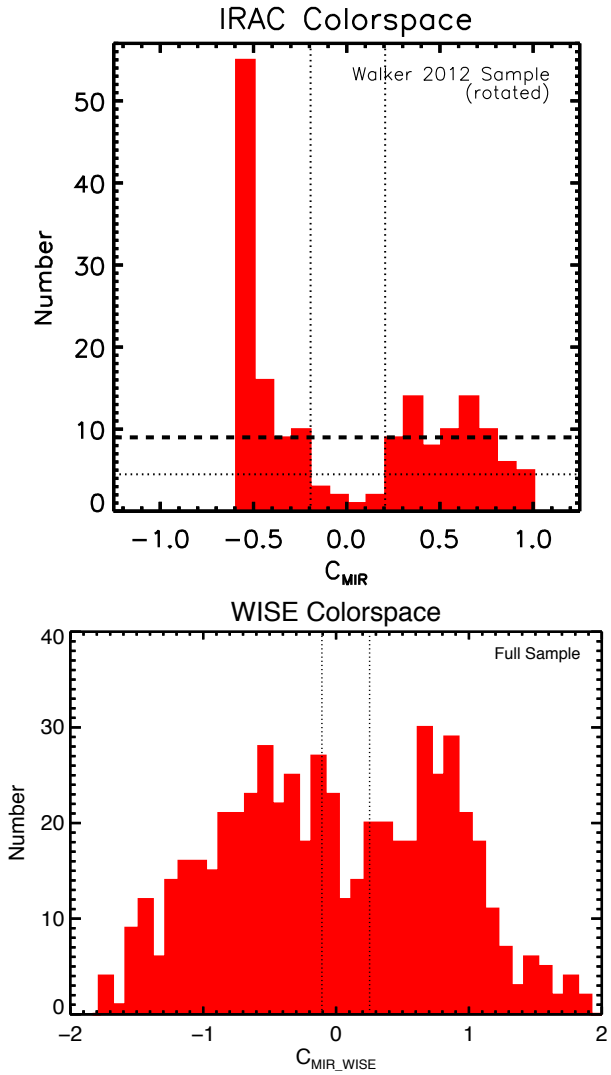

Fig. 3.— Rotated colorspace distribution of the Walker et al. (2012) sample (top), along with our full sample (bottom). In each case, a straight line fit to the colorspace distribution of the corresponding sample became the axis. For the Walker et al. (2012) IRAC sample, the dashed line indicates the median number per bin, with the horizontal dotted line half that value; the vertical dotted lines indicate the boundaries of the canyon, defined to be where the distribution is less than half the median value. Though we do not use the histogram to define the canyon, we also indicate the region corresponding to the new WISE canyon with vertical dotted lines.

3.3. Star Formation Rate and Stellar Mass

The WISE bands have proven to be excellent probes of both star formation rate and total stellar mass content, two critical parameters needed to understand the formation and evolution of galaxies. Evolved stellar populations emit the majority of their light at near-infrared wavelengths ($1-5\mu$m), so both the (W1) 3.4μm and (W2) 4.6μm bands effectively trace photospheric emission from these older stars; W1 is particular sensitive to stellar light, and can often observe luminosities on the order of $L_\star$ out to $z \approx 0.5$ (Cluver et al. 2014). The W1 and W2 bands are optimal tracers of the stellar mass content because they suffer minimally from extinction and can detect the Rayleigh Jeans tail for stars hotter than 2000 K (Jarrett et al. 2013). We use Eq. (9) from Jarrett et al. (2013) to derive our stellar masses: $\log(\frac{M_*}{L_{W1}})(\frac{M_\odot}{L_\odot}) = -0.246 - 2.100(W1 - W2)$, where W1 and W2 are given in magnitudes and L_{W1} is the total "in-band" luminosity, derived by multiplying the spectral luminosity, $\nu L_{3.4}$, by a factor of 22.883; as explained in Jarrett et al. (2013), this factor accounts for the difference between the total solar luminosity and the in-band values as measured by WISE. We convert from flux densities (Jy) to magnitudes using the relationship $m_{\rm vega} = -2.5\log_{10}[\frac{f_\nu}{f_{\nu 0}}]$, with $f_{\nu 0}$ given by 306.682 Jy, 170.663 Jy, 29.0448 Jy, and 8.2839 Jy for bands W1, W2, W3, and W4 respectively (see Table 1 in §IV.4 of the WISE All-Sky Explanatory Supplement[4]). Similarly, we calculate global star formation rates using far-infrared thermal emission (probed by the W4 22μm band), as a sizable fraction of this emission is powered by young stars. We use Eq. (2) from Jarrett et al. (2013) to calculate our star formation rates: SFR_{IR} ($M_\odot$ yr^{-1}) $= 7.50 \times 10^{-10} \nu L_{22}$ ($L_\odot$), where the spectral luminosity has been normalized by $L_\odot$ (3.839×10^{33} erg s^{-1}). In all cases, luminosities are derived assuming a distance of $d = 4280\ Mpc \times z$, the same distance estimation SDSS recommends for the conversion of SDSS apparent magnitudes to absolute magnitudes.[5]

In Figure 4, we show $\log[\frac{f_{22}}{f_{3.4}}]$ vs. $\log[M_*]$ (effectively sSFR vs. stellar mass) and $\log[\frac{f_{22}}{f_{3.4}}]$ vs. log[SFR] for our full sample. In both cases, the galaxies are color-coded by their location in WISE color-color space. We note that the WISE quiescent, canyon, and active galaxies from the full sample span approximately the same range in stellar mass ($\approx 10^8 - 10^{11.5}$ $M_\odot$), but the quiescent galaxies (median M_* of $10^{10.59}$ $M_\odot$) tend to have systematically higher stellar masses than the WISE canyon galaxies (median M_* of $10^{10.34}$ $M_\odot$), while the WISE canyon galaxies have systematically higher stellar masses than the WISE active galaxies (median M_* of $10^{9.92}$ $M_\odot$). We also find that the star formation rates of active, canyon, and quiescent galaxies overlap, but that the median of each class is shifted, with the active galaxies predictably having the highest median star formation rate (0.65 $M_\odot$ yr^{-1}), followed by the canyon galaxies (0.27 $M_\odot$ yr^{-1}) and the quiescent galaxies (0.09 $M_\odot$ yr^{-1}). For the full sample, our star formation rates span $\approx 0.001 - 10.0$ $M_\odot$ yr^{-1}.

---

[4]http://wise2.ipac.caltech.edu/docs/release/allsky/expsup/sec4_4h.html

[5]http://skyserver.sdss.org/dr12/en/help/cooking/general/getdata5.aspx

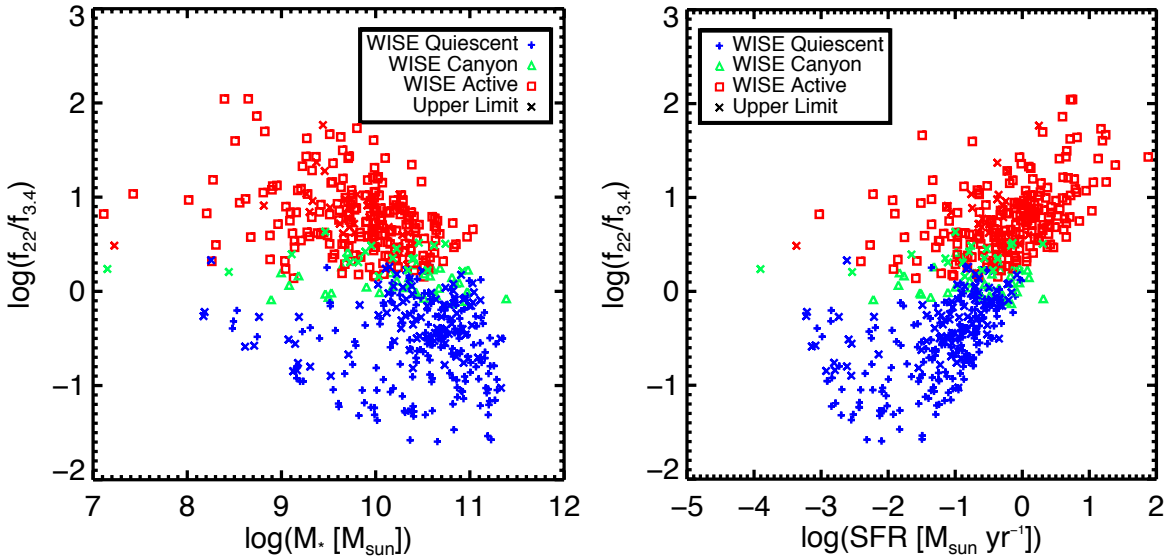

Fig. 4.— We show *Left:* $\log[\frac{f_{22}}{f_{3.4}}]$ vs. $\log[M_*]$ and *Right:* $\log[\frac{f_{22}}{f_{3.4}}]$ vs. log[SFR] for our full sample, with the galaxies color-coded by their location in WISE color-color space. Galaxies with an upper limit in either W3 or W4 (see Figure 2) are color-coded by the same classification but plotted with X's.

3.4. Morphology

In order to better understand the physical origins of the WISE canyon, in Figure 5 we plot the distribution of galaxy morphologies in WISE colorspace. The morphologies are from the HyperLeda[6] database (Paturel et al. 2003a,b), which accumulates morphologies from available publications and compares and combines them to determine an optimal De Vaucouleurs number for each galaxy. In our classification scheme, an average De Vaucouleurs number between -5.0–0.50 was assigned a morphology of E–S0/a. Similary, 0.50–2.50=Sa–Sab, 2.50–4.50=Sb–Sbc, 4.50–7.50=Sc–Sd, and 7.50–10.0=Irr,Sdm. In concordance with Alatalo et al. (2014), we see a significant bifurcation between spirals and bulge-dominated galaxies in this distinct region of WISE color-color space: the quiescent region is dominated by elliptical and S0 galaxies, while the majority of Sc–Sd spiral and irregular galaxies occupy the active region. Excluding those with upper limits, the canyon galaxies between these two populations exhibit a diverse range of morphologies, but is dominated in almost equal numbers by Sa-Sbc types (16 galaxies) and Elliptical/S0 types (13 galaxies). The rest of the canyon galaxies with reliable photometry are a mix of Sc-Sd type (4 galaxies) and irregulars (4 galaxies). A large fraction of the upper limit canyon galaxies (17/20 galaxies) are Elliptical/S0s, and would produce a canyon that is overwhelmingly early type if included in this analysis. The

[6]http://leda.univ-lyon1.fr/leda/rawcat/a102.html

abundance of Sa-Sbc type galaxies in the higher signal-to-noise canyon region is not surprising, as these galaxies tend to have brighter mid-IR-blue bulges than Sc-Sd type galaxies (Jarrett 2000). When combined with their actively to moderately star-forming mid-IR-green and red disks, this combination would be expected to produce green mid-IR colors indicative of moderate star formation.

In Figure 6, we show optical, five-color SDSS thumbnails[7] alongside their WISE three-color thumbnails[8] for all the WISE canyon galaxies with reliable photometry ($SNR > 2$ in all four bands) in the SDSS DR12 footprint (31 of 37 total canyon galaxies). Of the 31 reliable canyon galaxies within the SDSS footprint, 11 show visible signs of gravitational interaction with a neighboring companion in their WISE thumbnail. Moreover, the combination of mid-IR blue bulges and mid-IR red star-forming disks is apparent in a number of the WISE thumbnails (for example, HCG22c, HCG45a, HCG69a, HCG71a, HCG88a, NGC0070, NGC4274). Interestingly, several galaxies show the opposite color combination (mid-IR red nucleus and mid-IR blue outskirts), including HCG37b, NGC4117, and NGC4314.

---

[7]http://skyserver.sdss.org/dr12/en/tools/chart/listinfo.aspx

[8]https://irsa.ipac.caltech.edu/applications/wise/

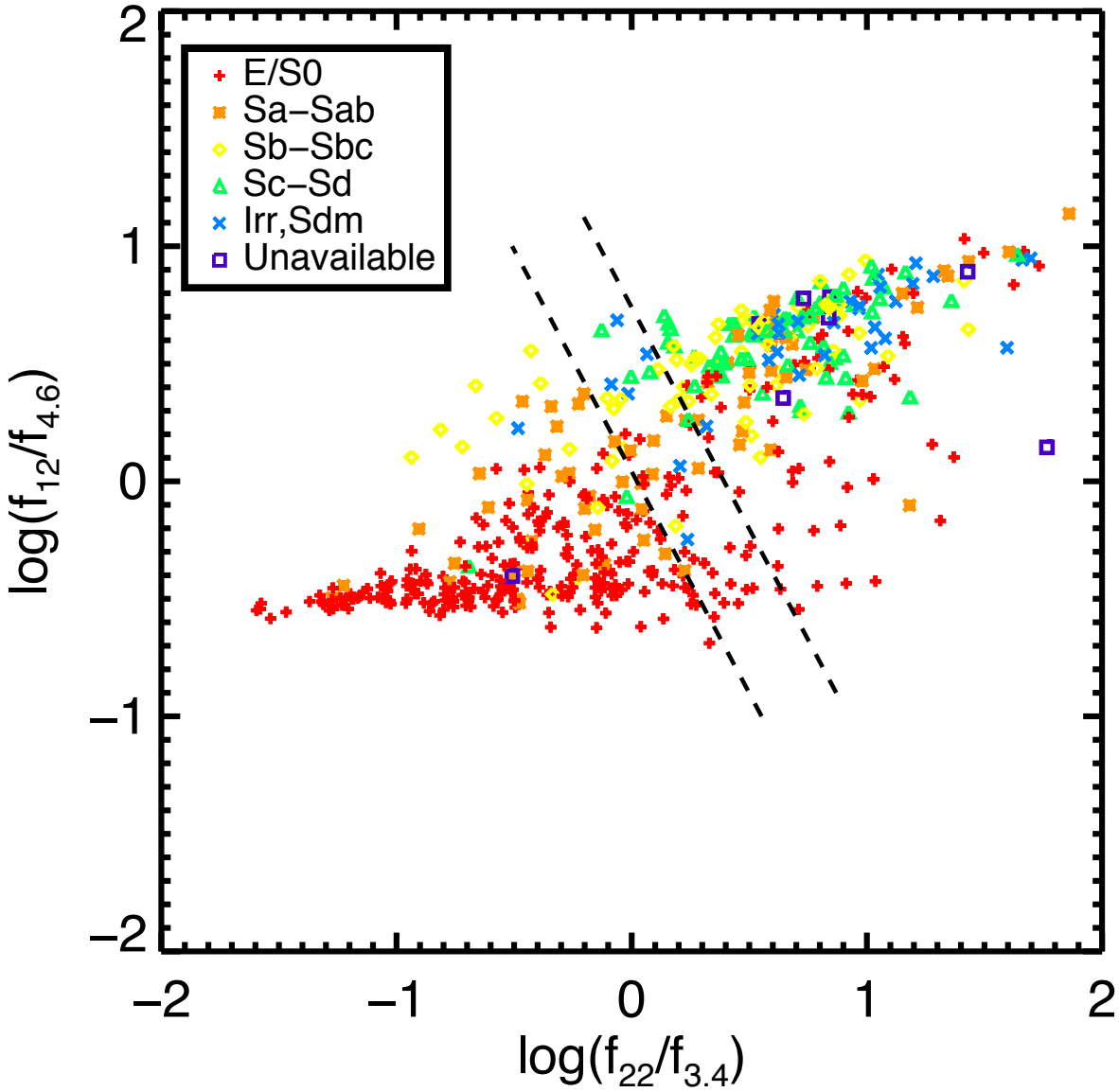

Fig. 5.— Distribution of compact group galaxy morphologies from the full sample in WISE mid-IR colorspace. The boundaries of the canyon are marked with dashed lines. As expected, elliptical and S0 galaxies dominate the quiescent region, while Sc–Sd galaxies dominate the active region. Sa–Sbc types (16 galaxies) and Elliptical/S0 types (13 galaxies) dominate the moderately star forming WISE canyon region, though there is also a small number of Sc-Sd and irregular types (8 galaxies). The lone Sc-Sd galaxy in the quiescent region (IC0107) appears to be an errant misclassification of the galaxy by the HyperLeda morphology compiler, as it morphologically resembles an elliptical galaxy.

WISE-SDSS Thumbnail Comparison

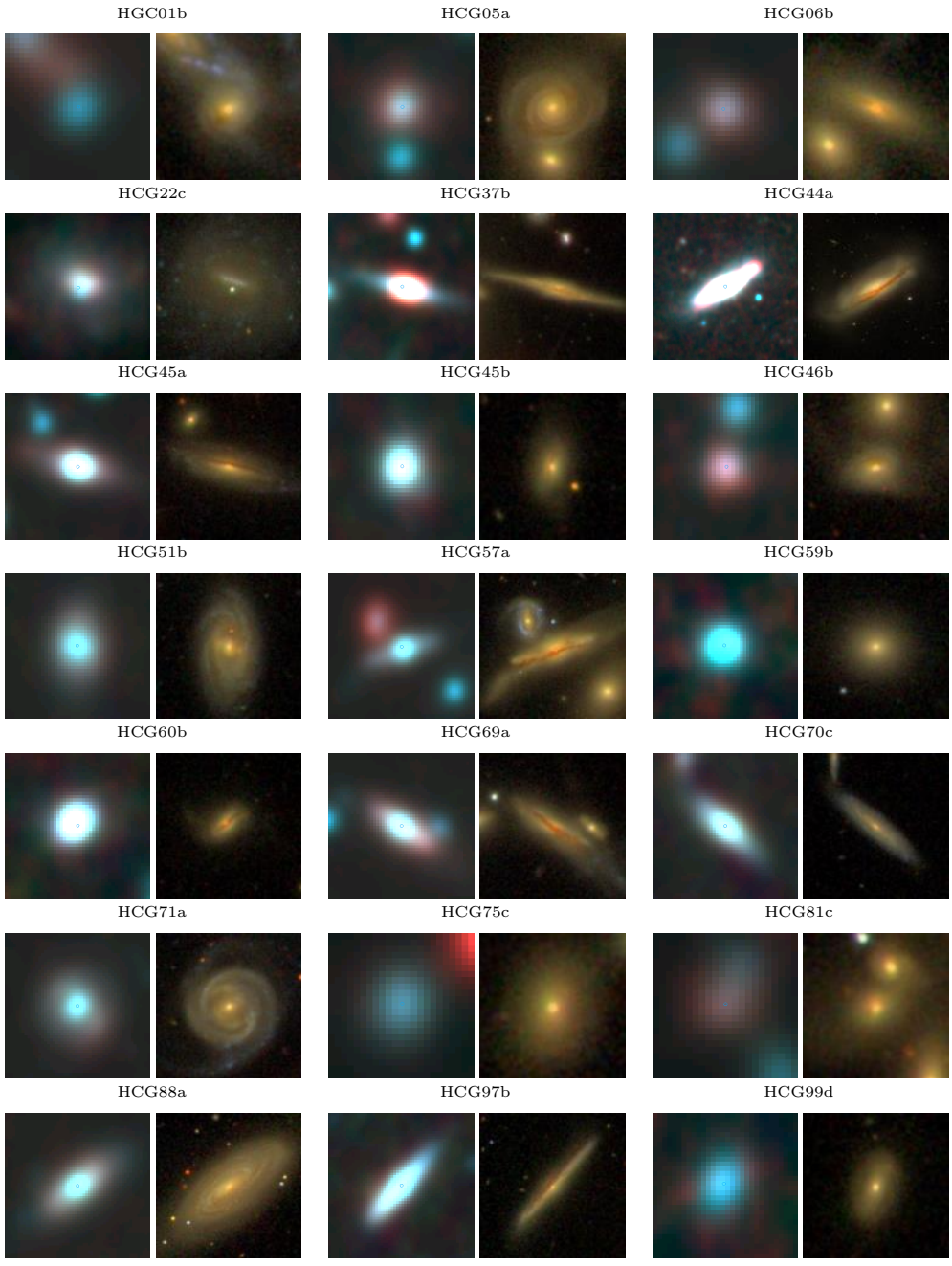

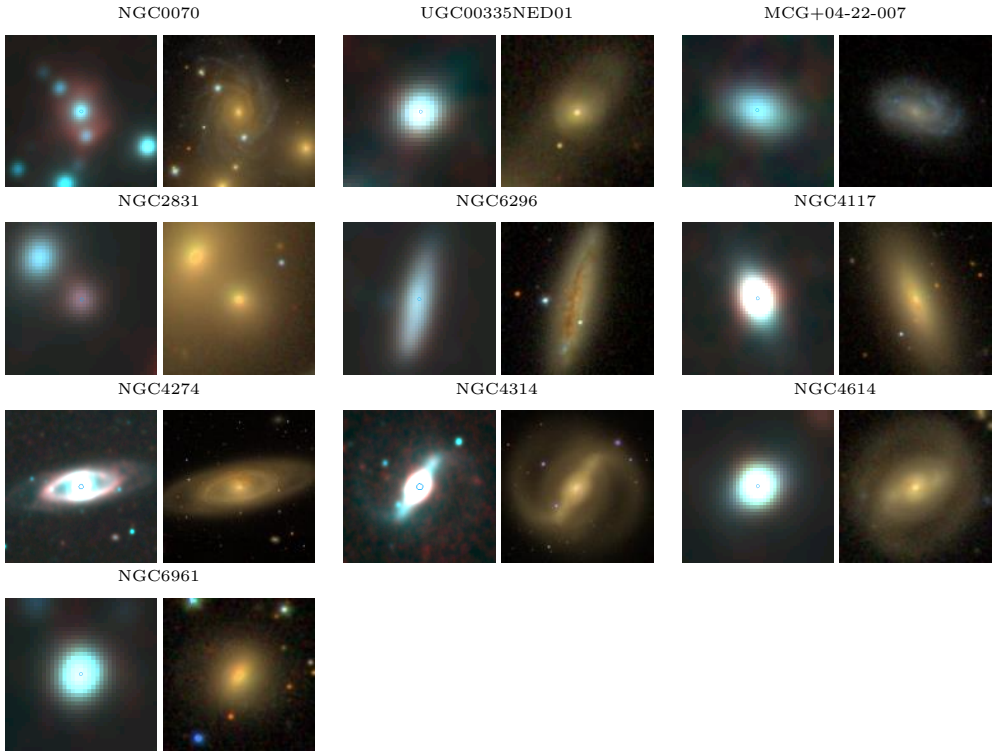

Fig. 6.— Side-by-side comparison of *Left:* Five-color [*ugriz*] SDSS thumbnails and *Right:* Three-color [3.4μm (blue), 4.6μm (green), 12μm (red)] composite WISE thumbnails of all the $SNR > 2$ galaxies in the WISE canyon that fall within the SDSS footprint (31 galaxies). The size scale in each pair is identical and the scales range from $30'' - 360''$ over all thumbnails. The median PSF (r band) of the SDSS cutouts is 1.3", while the typical PSF (3.4μm, 4.6μm, 12μm bands) for the WISE cutouts is 8.5". In the WISE images, red indicates active star formation while blue indicates quiescence, while the opposite is true in the SDSS images.

3.5. WISE-SDSS Colorspace

As seen in Figure 7, we also confirm a relation between $\log[\frac{f_{12}}{f_{4.6}}]$ vs. [u-r] color for compact group galaxies, a relation first noted for Galaxy Zoo sources in Alatalo et al. (2014). They find a significant bifurcation between late-type (blue contours) and early-type (red contours) galaxies; the green valley galaxies (cyan contours) appear at the elbow of the two distributions. The Alatalo et al. (2014) contours are derived by plotting $\approx 50,000$ field galaxies in this region of colorspace, which are characterized as either "early", "late", or "green valley" objects in Galaxy

Zoo. We plot the 407 galaxies from the full sample that fall within the SDSS footprint, and overlay the same contours as Figure 1f in Alatalo et al. (2014), now uncorrected for intrinsic extinction. Alatalo et al. (2014) originally correct for intrinsic extinction using the $E(B-V)_{stars}$ from the Oh et al. (2011) OSSY catalog, which is then converted to an extinction measure at the rest wavelength of the galaxy. The OSSY database is derived from the SDSS DR7 spectral catalog, and only $\approx 2/3$ of our sample have SDSS spectral data; thus, we are not able to correct for intrinsic extinction following the methodology from Alatalo et al. (2014). As a subset of our sample tends to be both dusty and actively star forming, correcting for intrinsic extinction would preferentially shift our active population towards lower [u-r] color, and the kink in the distribution would become more pronounced.

When comparing the photometry, we find an offset between the Galaxy Zoo [W2-W3] colors and our compact group [W2-W3] colors. The Galaxy Zoo magnitudes are composed largely of the w2gmag and w3gmag parameters in the ALLWISE source catalog, whose elliptical apertures are scaled from the 2MASS extended source catalog apertures. Specifically, the ALLWISE gmag aperture semi-major axes are 1.1 times the 2MASS XSC K_s circular semi-major axes. When directly comparing the subsample of our compact group galaxies that are also Galaxy Zoo objects, we find a net offset of $\approx 0.3-0.4$ magnitudes between the two samples. We attribute this offset to a difference in aperture type: the gmag elliptical apertures are determined using solely the 2.159μm 2MASS K_s image, while are custom $1-3\sigma$ contour apertures are determined using an averaged, λ^{-1} weighted reference image composed of the 3.4μm, 4.6μm, and 12μm images. Our offset is consistent with the findings of Cluver et al. (2014), who quantify the difference between WISE gmag and isophotal photometry and determine a shift of $\approx 0.2-0.4$ magnitudes. The gmag apertures can also be contaminated by neighboring sources, which likely produces higher gmag values for faint sources when compared directly to the isophotal photometry (Cluver et al. 2014). Nevertheless, the shift is not significant with regards to our conclusions, and we note the same bifurcation between "active" compact group galaxies (dominated by late-type Sc-Sd galaxies, see Figure 5) and "quiescent" compact group galaxies (dominated by early-type E/S0 galaxies). We also find that the WISE IR canyon galaxies cluster near the "elbow" between the early-type (lower right red contours) and late-type (upper left blue contours) galaxy distributions, though they do tend to span a larger range in [W2-W3] color. We also note a dearth of canyon galaxies within the optical green valley (cyan contours), reconfirming that WISE infrared canyon galaxies *do not fall in the optical green valley.* Instead, as argued in Walker et al. (2013), we confirm that the majority of our WISE canyon galaxies tend to be optically redder than typical green valley objects in Galaxy Zoo, falling on or near the red sequence.

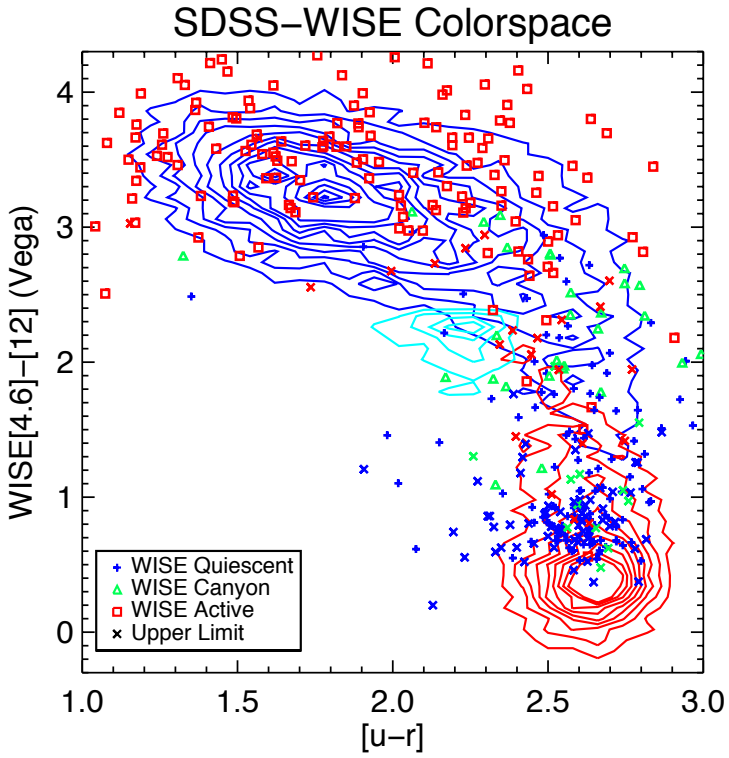

Fig. 7.— Distribution of compact group galaxies in $\log[\frac{f_{12}}{f_{4.6}}]$ vs. [u-r] color, with contours (now uncorrected for intrinsic extinction) from Alatalo et al. (2014) overlaid. The galaxies are color-coded by their location in WISE color-color space; galaxies with an upper limit in either W3 or W4 (see Figure 2) are color-coded by the same classification but plotted with X's. We confirm a bimodality between morphologically classified early-type (red contours) and late-type (blue contours) galaxies, first seen for field galaxies in Alatalo et al. (2014), but here for compact group galaxies, with a majority of our WISE canyon galaxies falling at the elbow of the two distributions. We also note a dearth of WISE canyon galaxies within the optical green valley (cyan contours).

4. Summary and Conclusions

We perform custom photometry on a comprehensive sample of 163 compact groups and produce a catalog of 567 compact group galaxies in all four WISE bands. Within this sample, we present the identification of 37 moderately star-forming WISE canyon galaxies which reliable photometry that lie in a distinct region of WISE $\log[\frac{f_{12}}{f_{4.6}}]$ vs. $\log[\frac{f_{22}}{f_{3.4}}]$ color-color space. Canyon galaxies are severely under-represented in the previous *Spitzer* sample, and the small number statistics prevent an understanding of the dominant evolutionary mechanisms at play. With this enlarged sample, it should be possible to begin statistically characterizing the properties of the WISE canyon galaxies, and to examine what processes may be causing their accelerated

evolution. We also note that, despite the WISE canyon region being less pronounced than the *Spitzer* IRAC canyon, we can also utilize this WISE colorspace to separate galaxies dominated by stellar light from galaxies dominated by PAH and thermal emission. The creation of a photometric catalog could aid future studies seeking to characterize the properties of these unique galaxies and their accelerated evolution.

We also note distinct trends between WISE classification [quiescent, canyon, active] and both stellar mass and star formation rate. Though the classes span approximately the same range of stellar masses, the WISE quiescent class tends to have systematically higher stellar masses than the canyon class, while the canyon class has systematically higher stellar masses than the active class. The opposite is predictably true for star formation rate: though the classes overlap in SFR space, the active class has the highest median SFR, followed by the canyon class and the quiescent class.

Similar to Alatalo et al. (2014), we find that compact group galaxies also exhibit a bimodality between early and late type galaxies in WISE $\log[\frac{f_{12}}{f_{4.6}}]$ vs. $\log[\frac{f_{22}}{f_{3.4}}]$ color-color space, with a plurality of WISE narrow canyon galaxies being of type Sa-Sbc. However, we note that the canyon between spiral and bulge-dominated galaxies does not correspond to the optical green valley and confirm the results from Walker et al. (2013) that a majority of WISE canyon galaxies tend to be optically redder.

Ultimately, this statistical sample provides a means to address how galaxies are transformed in the high-density and dynamically-evolving compact group environment, and consequently what impact this key environment has on galaxy evolution and hierarchical formation. A number of processes could be responsible for this accelerated evolution—possibilities include briefly enhanced star formation due to a tidal inflow of gas; rapidly quenched star formation to the tidal removal of gas; or strangulation if cool filaments of gas are not able to refuel the system. Determining the relative importance of these and other mechanisms is essential to understanding how the gas is processed in these groups, which has a direct impact on the resulting merger products.

5. Acknowledgments

This publication makes use of data products from the Wide-field Infrared Survey Explorer, which is a joint project of the University of California, Los Angeles, and the Jet Propulsion Laboratory/California Institute of Technology, funded by the National Aeronautics and Space Administration

Funding for the Sloan Digital Sky Survey IV has been provided by the Alfred P. Sloan Foundation, the U.S. Department of Energy Office of Science, and the Participating Institutions. SDSS-IV acknowledges support and resources from the Center for High-Performance Computing at the University of Utah. The SDSS web site is www.sdss.org.

Catherine S. Zucker would like to sincerely thank the anonymous referee for their thorough feedback throughout the review process. She would also like to thank the Virginia Space Grant Consortium and the University of Virginia College of Arts and Sciences for support.

Sarah C. Gallagher thanks the Natural Sciences and Engineering Research Council of Canada for support.

REFERENCES

Alatalo, K., Cales, S. L., Appleton, P. N., et al. 2014, ApJ, 794, L13

Aniano, G., Draine, B. T., Gordon, K. D., & Sandstrom, K. 2011, Publications of the Astronomical Society of the Pacific, 123, 1218

Appleton, P. N., Xu, K. C., Reach, W., et al. 2006, ApJL, 639, L51

Assef, R. J., Kochanek, C. S., Brodwin, M., et al. 2010, ApJ, 713, 970

Barton, E., Geller, M., Ramella, M., Marzke, R. O., & da Costa, L. N. 1996, The Astronomical Journal, 112, 871

Barton, E. J., de Carvalho, R. R., & Geller, M. J. 1998, The Astronomical Journal, 116, 1573

Blanton, M. R., Lupton, R. H., Schlegel, D. J., et al. 2005, ApJ, 631, 208

Chilingarian, I. V., & Zolotukhin, I. Y. 2012, Monthly Notices of the Royal Astronomical Society, 419, 1727

Cluver, M. E., Appleton, P. N., Boulanger, F., et al. 2010, ApJ, 710, 248

Cluver, M. E., Appleton, P. N., Ogle, P., et al. 2013, ApJ, 765, 93

Cluver, M. E., Jarrett, T. H., Hopkins, A. M., et al. 2014, ApJ, 782, 90

Galliano, F., Madden, S. C., Tielens, A. G. G. M., Peeters, E., & Jones, A. P. 2008, ApJ, 679, 310

Hickson, P. 1982, ApJL, 255, 382

Hickson, P., de Oliveira, C. M., Huchra, J. P., & Palumbo, G. G. 1992, ApJL, 399, 353

Jarrett, T. H. 2000, Publications of the Astronomical Society of the Pacific, 112, 1008

Jarrett, T. H., Cohen, M., Masci, F., et al. 2011, ApJ, 735, 112

Jarrett, T. H., Masci, F., Tsai, C. W., et al. 2013, The Astronomical Journal, 145, 6

Johnson, K. E., Hibbard, J. E., Gallagher, S. C., et al. 2007, AJ, 134, 1522

Konstantopoulos, I. S., Maybhate, A., Charlton, J. C., et al. 2013, ApJ, 770, 114

Lang, D. 2014, The Astronomical Journal, 147, 108

Oh, K., Sarzi, M., Schawinski, K., & Yi, S. K. 2011, ApJS, 195, 13

Paturel, G., Petit, C., Prugniel, P., et al. 2003a, Astronomy and Astrophysics, 412, 45

Paturel, G., Theureau, G., Bottinelli, L., et al. 2003b, Astronomy and Astrophysics, 412, 57

Reines, A. E., Johnson, K. E., & Goss, W. M. 2008, The Astronomical Journal, 135, 2222

Sadjadi, S., Zhang, Y., & Kwok, S. 2015, ApJ, 807, 95

Schlegel, D. J., Finkbeiner, D. P., & Davis, M. 1998, ApJ, 500, 525

Tzanavaris, P., Hornschemeier, A. E., Gallagher, S. C., et al. 2010, ApJ, 716, 556

Tzanavaris, P., Gallagher, S. C., Hornschemeier, A. E., et al. 2014, ApJS, 212, 9

Walker, L. M., Johnson, K. E., Gallagher, S. C., et al. 2012, The Astronomical Journal, 143, 69

—. 2010, The Astronomical Journal, 140, 1254

Walker, L. M., Butterfield, N., Johnson, K., et al. 2013, ApJ, 775, 129

Wright, E. L., Eisenhardt, P. R. M., Mainzer, A. K., et al. 2010, The Astronomical Journal, 140, 1868

Wu, Y., Helou, G., Armus, L., et al. 2010, ApJ, 723, 895

Wyder, T. K., Martin, D. C., Schiminovich, D., et al. 2007, The Astrophysical Journal Supplement Series, 173, 293

6. Appendix

6.1. Canyon Bounds

Quantitatively, we define our canyon zone to be where:

$$\text{ywise} \geq (0.01866 - 1.885 \times \text{xwise}) \wedge \text{ywise} \leq (0.7844 - 1.885 \times \text{xwise})$$

where xwise=$\log[\frac{f_{22}}{f_{3.4}}]$ color and ywise=$\log[\frac{f_{12}}{f_{4.6}}]$ color

Table 1. WISE Galaxies from Full Sample

Group	Galaxy	W1 mJy	W2 mJy	W3 mJy	W4 mJy	Morphology	De Vaucouleurs number*	WISE Class**	Photometry type***	Upper Limit****
HCG01	a	3.43±0.08	2.04±0.05	7.59±0.22	22.50±1.45	Sc	6.0	Active	3	No
HCG01	b	4.06±0.09	2.15±0.05	1.96±0.14	6.92±1.02	E	-3.5	Canyon	3	No
HCG01	c	3.54±0.06	1.82±0.04	0.67±0.02	3.42±6.54	E-S0	-3.4	Quiescent	2	Yes
HCG01	d	0.95±0.05	0.49±0.03	0.55±0.02	4.86±4.78	S0	-1.9	Active	2	Yes
HCG02	a	9.42±0.09	6.11±0.07	33.18±0.17	87.30±1.52	SBd	8.0	Active	1	No
HCG02	b	11.90±0.05	8.49±0.03	79.40±0.07	373.56±7.72	S0-a	-1.1	Active	2	No
HCG02	c	5.56±0.06	2.94±0.01	13.16±0.19	8.14±1.66	SABc	4.9	Active	2	No
HCG03	a	6.92±0.04	4.05±0.02	17.24±0.02	22.23±1.44	Sc	4.6	Active	2	No
HCG03	b	7.17±0.04	3.67±0.02	1.18±0.06	3.85±2.48	S0-a	-0.7	Quiescent	2	Yes
HCG03	d	4.96±0.02	2.52±0.00	0.97±0.02	3.46±34.09	S0	-2.2	Quiescent	2	Yes
HCG04	a	28.82±0.14	21.33±0.13	166.23±0.30	420.68±3.24	SBc	5.0	Active	1	No
HCG04	c	4.11±0.06	2.26±0.03	1.50±0.05	3.84±2.76	E-S0	-3.3	Quiescent	2	Yes
HCG04	d	3.36±0.02	2.11±0.02	13.46±0.04	30.66±2.25	E-S0	-3.2	Active	2	No
HCG05	a	7.39±0.24	3.96±0.15	7.21±0.18	12.50±1.60	Sab	2.0	Canyon	2	No
HCG05	b	2.35±0.19	1.21±0.11	0.36±0.12	4.42±1.83	E	-3.7	Quiescent	2	No
HCG06	a	4.56±0.09	2.37±0.05	0.57±0.03	2.06±19.78	S0-a	-0.7	Quiescent	2	Yes
HCG06	b	2.84±0.11	1.58±0.07	1.79±0.08	5.46±0.99	Sa	1.3	Canyon	2	No
HCG06	c	1.71±0.12	0.93±0.05	0.39±0.05	2.60±6.03	E-S0	-3.2	Quiescent	2	Yes
HCG07	a	55.80±0.16	34.09±0.07	130.39±0.09	268.80±6.47	SBa	1.1	Active	2	No
HCG07	b	16.95±0.19	9.04±0.09	3.05±0.05	3.94±1.91	S0	-1.9	Quiescent	2	No
HCG07	c	24.59±0.07	13.81±0.04	54.11±0.22	35.08±1.51	Sc	5.0	Active	2	No
HCG07	d	3.08±0.07	1.76±0.04	5.41±0.11	9.81±1.29	S0-a	-1.4	Active	2	No
HCG08	a	6.36±0.20	3.33±0.11	0.97±0.10	2.03±0.75	E	-5.0	Quiescent	2	No
HCG08	b	3.34±0.11	1.76±0.07	1.25±0.06	5.52±3.28	S0	-2.0	Canyon	2	Yes
HCG08	c	2.99±0.20	1.57±0.10	0.85±0.02	2.46±4.58	S0	-2.0	Quiescent	2	Yes
HCG08	d	2.92±0.05	1.57±0.04	1.05±0.01	3.49±1.79	S0	-2.0	Quiescent	2	Yes
HCG10	a	57.21±0.46	31.00±0.22	43.53±0.16	10.89±0.96	Sb	3.1	Quiescent	2	No
HCG10	b	51.06±0.68	26.60±0.35	9.76±0.16	5.99±0.74	E-S0	-3.2	Quiescent	2	No
HCG10	c	11.13±0.05	5.89±0.02	1.68±0.05	57.12±1.79	S0-a	0.1	Active	2	No
HCG10	d	6.13±0.03	3.47±0.01	10.89±0.09	11.00±0.82	Sbc	3.6	Active	2	No
HCG12	a	10.71±0.11	5.65±0.07	1.96±0.03	3.36±3.42	S0	-2.3	Quiescent	2	Yes
HCG13	a	0.47±0.02	0.24±0.01	0.19±0.04	7.21±1.02	SBab	2.2	Active	2	No
HCG13	b	4.39±0.09	2.24±0.04	0.99±0.05	2.56±3.55	E	-5.0	Quiescent	2	Yes
HCG13	c	0.78±0.03	0.43±0.01	0.27±0.02	3.29±3.01	S0	-2.0	Active	2	Yes
HCG13	d	0.45±0.02	0.25±0.01	0.15±0.02	2.66±4.04	S0	-2.0	Active	2	Yes
HCG14	a	14.01±0.14	8.27±0.06	33.86±0.06	61.04±2.07	S0-a	-1.0	Active	2	No
HCG14	b	10.23±0.10	5.44±0.05	2.43±0.16	1.81±0.87	Sab	2.0	Quiescent	2	No
HCG14	c	3.09±0.05	1.82±0.03	4.45±0.06	9.81±0.83	S0-a	-0.5	Active	2	No
HCG15	a	16.45±0.19	8.85±0.10	7.93±0.10	5.96±1.07	S0	-1.8	Quiescent	2	No
HCG15	c	10.72±0.10	5.65±0.07	1.93±0.09	1.77±16.84	E-S0	-3.0	Quiescent	2	Yes
HCG15	d	6.11±0.07	3.52±0.05	2.78±0.08	4.81±0.97	E-S0	-3.0	Quiescent	2	No
HCG15	e	4.08±0.07	2.24±0.04	1.13±0.06	2.76±2.37	S0-a	-0.5	Quiescent	2	Yes
HCG15	f	1.09±0.07	0.60±0.05	2.28±0.03	4.27±0.91	Sab	1.6	Active	2	No
HCG16	a	64.46±0.38	40.52±0.24	201.15±0.32	383.16±0.58	Sab	1.9	Active	1	No
HCG16	b	27.33±0.40	14.87±0.20	11.37±0.20	17.26±1.02	Sa	0.8	Quiescent	2	No
HCG16	c	54.41±0.13	40.56±0.13	435.21±0.61	1412.78±3.20	S0-a	-1.1	Active	1	No
HCG16	d	39.38±0.16	35.71±0.07	338.93±0.37	1832.27±28.21	S0-a	-1.2	Active	2	No
HCG17	a	1.03±0.08	0.52±0.04	0.18±0.04	3.18±3.47	E	-4.2	Canyon	2	Yes
HCG17	b	3.73±0.13	1.92±0.07	0.81±0.03	3.00±4.04	E	-4.2	Quiescent	2	Yes
HCG19	a	15.75±0.14	8.48±0.07	2.28±0.09	2.41±1.95	E-S0	-3.1	Quiescent	2	Yes
HCG19	b	1.84±0.02	1.07±0.01	3.22±0.04	19.87±0.92	SBa	1.3	Active	2	No
HCG19	c	4.42±0.04	2.74±0.04	13.26±0.05	3.84±0.86	SBm	9.0	Canyon	2	No
HCG21	a	31.87±0.14	19.00±0.08	72.80±0.10	120.76±0.56	SBb	3.3	Active	1	No
HCG21	b	32.90±0.25	18.16±0.13	38.74±0.18	19.56±1.03	Sa	1.1	Quiescent	2	No
HCG21	c	28.83±0.28	15.09±0.15	5.16±0.07	2.64±0.66	E-S0	-3.2	Quiescent	2	No
HCG22	a	100.52±0.88	52.62±0.49	18.37±0.17	7.56±0.91	E	-4.8	Quiescent	2	No
HCG22	c	6.44±0.18	3.60±0.07	8.47±0.14	6.23±0.90	Sd	7.9	Canyon	2	No
HCG23	a	30.94±0.10	17.07±0.05	19.26±0.09	8.21±0.82	S0-a	-0.6	Quiescent	2	No
HCG23	b	30.11±0.25	18.35±0.10	81.12±0.47	109.54±0.43	Sab	1.7	Active	1	No
HCG23	c	15.98±0.06	9.35±0.03	6.97±0.02	17.89±0.84	S0-a	-0.6	Quiescent	2	No
HCG23	d	6.42±0.04	4.04±0.01	22.85±0.06	56.65±1.66	Sc	6.1	Active	2	No
HCG24	a	6.62±0.13	3.47±0.07	1.34±0.03	2.66±3.56	S0	-2.0	Quiescent	2	Yes
HCG24	b	10.11±0.09	5.44±0.07	3.03±0.10	3.80±3.23	SBa	1.0	Quiescent	2	Yes
HCG24	c	1.10±0.06	0.60±0.04	0.22±0.01	2.91±3.89	S0	-2.0	Canyon	2	Yes
HCG25	a	7.54±0.05	4.83±0.02	29.88±0.19	54.23±0.52	SBbc	4.2	Active	1	No
HCG25	b	14.13±0.09	7.83±0.06	8.47±0.02	7.67±1.19	SBa	0.9	Quiescent	2	No

Table 1—Continued

Group	Galaxy	W1 mJy	W2 mJy	W3 mJy	W4 mJy	Morphology	De Vaucouleurs number*	WISE Class**	Photometry type***	Upper Limit****
HCG26	a	4.54±0.10	3.08±0.06	13.46±0.28	22.96±1.16	Sc	5.5	Active	3	No
HCG26	e	0.38±0.01	0.26±0.00	1.49±0.03	5.01±0.94	I	10.0	Active	2	No
HCG27	c	1.99±0.02	1.21±0.01	2.28±0.06	2.81±1.03	Sa	1.0	Canyon	2	No
HCG27	d	0.70±0.02	0.43±0.01	0.78±0.02	2.77±6.22	S0	-2.0	Active	2	Yes
HCG27	e	0.48±0.01	0.31±0.00	1.01±0.02	2.59±0.99	S0	-2.0	Active	2	No
HCG27	f	0.07±0.00	0.04±0.00	0.06±0.00	4.03±2.43	-	-	Active	2	Yes
HCG28	a	6.66±0.08	3.98±0.04	5.54±0.04	6.05±1.02	Sb	3.0	Canyon	2	No
HCG28	c	2.32±0.04	1.25±0.02	0.42±0.06	5.23±6.07	S0	-2.3	Canyon	2	Yes
HCG29	b	1.34±0.04	0.88±0.03	2.93±0.14	8.32±0.81	S0	-1.9	Active	3	No
HCG29	c	0.97±0.03	0.57±0.02	0.30±0.11	3.12±1.93	E	-4.2	Canyon	3	Yes
HCG30	a	16.96±0.35	8.95±0.21	2.62±0.12	3.51±1.03	S0-a	-0.7	Quiescent	2	No
HCG30	b	26.11±0.20	13.97±0.08	11.23±0.11	7.87±1.05	S0-a	-1.1	Quiescent	2	No
HCG30	c	2.26±0.04	1.30±0.02	3.80±0.06	9.49±1.25	SBbc	3.6	Active	2	No
HCG31	c	4.44±0.10	4.43±0.09	72.12±0.97	489.22±9.10	I	10.0	Active	3	No
HCG32	a	6.79±0.18	3.56±0.09	1.17±0.03	2.97±1.72	E	-3.9	Quiescent	2	Yes
HCG32	b	4.30±0.04	2.32±0.01	1.18±0.08	3.10±3.15	S0-a	-0.8	Quiescent	2	Yes
HCG32	c	2.17±0.08	1.22±0.04	2.22±0.09	4.17±2.33	Sa	1.1	Active	2	Yes
HCG32	d	1.14±0.17	0.61±0.14	0.55±0.03	3.27±0.89	S0	-2.0	Active	2	No
HCG33	a	9.36±0.24	4.99±0.13	2.08±0.02	3.84±1.04	E	-4.4	Quiescent	2	No
HCG33	b	9.57±0.40	5.20±0.22	2.22±0.05	3.11±1.13	E	-3.6	Quiescent	2	No
HCG33	c	12.82±0.21	7.71±0.10	22.35±0.14	29.33±0.79	Sc	5.5	Active	1	No
HCG34	a	14.34±0.19	7.75±0.10	4.74±0.09	18.56±1.22	E	-3.9	Quiescent	2	No
HCG34	b	3.80±0.06	2.91±0.04	17.51±0.12	37.52±2.42	E-S0	-3.0	Active	2	No
HCG34	c	0.35±0.07	0.25±0.05	1.90±0.26	3.97±0.55	SBd	8.0	Active	1	No
HCG35	a	2.76±0.05	1.45±0.02	0.64±0.03	2.11±0.97	Sab	2.3	Quiescent	2	No
HCG35	b	4.10±0.09	2.15±0.05	0.98±0.00	4.01±2.33	E	-3.9	Quiescent	2	Yes
HCG35	c	3.58±0.06	1.83±0.03	0.67±0.05	2.72±3.70	E-S0	-3.3	Quiescent	2	Yes
HCG35	d	1.72±0.03	1.00±0.02	1.56±0.02	5.56±3.26	Sb	3.0	Active	2	Yes
HCG35	e	0.18±0.04	0.10±0.02	0.15±0.01	3.34±3.12	S0	-1.9	Active	2	Yes
HCG37	a	30.17±0.67	15.38±0.32	5.77±0.01	4.04±1.32	E	-4.8	Quiescent	2	No
HCG37	b	15.50±0.31	9.14±0.22	19.07±0.09	22.68±1.55	Sb	3.4	Canyon	2	No
HCG37	d	0.58±0.02	0.34±0.01	1.56±0.05	3.26±1.07	S?	4.1	Active	2	No
HCG37	e	0.48±0.02	0.25±0.01	0.30±0.03	3.31±4.68	E-S0	-3.3	Active	2	Yes
HCG38	a	8.17±0.04	5.26±0.03	28.91±0.03	41.79±1.49	Sb	2.7	Active	2	No
HCG38	b	2.80±0.16	1.92±0.10	13.73±0.48	72.50±2.80	SBbc	4.1	Active	2	No
HCG38	c	1.18±0.06	0.85±0.04	6.70±0.38	25.14±3.01	S?	2.4	Active	1	No
HCG39	a	0.90±0.05	0.51±0.03	0.64±0.03	3.18±1.09	Sb	3.0	Active	2	No
HCG39	b	0.23±0.02	0.12±0.01	0.08±0.02	4.62±1.20	E-S0	-2.8	Active	2	No
HCG39	c	0.90±0.01	0.60±0.01	3.28±0.06	14.70±1.31	S?	1.9	Active	2	No
HCG39	d	0.40±0.01	0.21±0.01	0.21±0.03	4.27±2.90	S0	-1.9	Active	2	Yes
HCG40	a	21.23±0.25	11.29±0.14	3.49±0.07	3.70±2.73	E	-4.8	Quiescent	2	Yes
HCG40	b	10.25±0.21	5.34±0.11	3.10±0.16	6.53±1.21	E-S0	-3.0	Quiescent	3	No
HCG40	c	13.42±0.62	8.53±0.36	36.05±0.34	49.68±1.01	SBab	2.3	Active	1	No
HCG40	d	14.53±0.34	8.99±0.11	36.32±0.14	90.44±1.98	S0-a	0.1	Active	2	No
HCG40	e	2.09±0.05	1.12±0.03	1.52±0.13	8.16±1.01	SABa	1.3	Active	3	No
HCG42	a	123.29±1.46	64.98±0.83	19.84±0.10	6.02±0.96	E	-4.8	Quiescent	2	No
HCG42	c	17.37±0.31	9.31±0.20	3.09±0.06	2.14±0.87	E	-4.6	Quiescent	2	No
HCG43	a	6.33±0.02	3.93±0.02	16.13±0.03	29.63±1.60	Sb	2.8	Active	2	No
HCG43	b	3.49±0.01	2.27±0.01	13.38±0.08	26.63±1.24	SBc	4.7	Active	2	No
HCG43	c	3.78±0.02	1.92±0.01	0.77±0.01	3.11±30.52	S0-a	-0.5	Quiescent	2	Yes
HCG43	d	0.71±0.02	0.41±0.01	0.81±0.03	3.72±12.04	Sc	6.0	Active	2	Yes
HCG43	e	1.07±0.01	0.61±0.01	0.27±0.02	2.17±20.19	E-S0	-3.5	Canyon	2	Yes
HCG44	a	280.08±0.83	157.02±0.47	231.66±0.09	237.37±0.57	Sa	0.9	Canyon	1	No
HCG44	b	130.08±1.60	68.02±0.88	20.22±0.43	7.83±1.63	E	-4.8	Quiescent	2	No
HCG44	c	57.46±0.41	32.65±0.21	86.00±0.31	121.18±2.64	Sa	1.2	Active	2	No
HCG44	d	11.66±0.16	7.07±0.07	35.89±0.06	16.04±1.55	SBc	5.0	Active	2	No
HCG45	a	7.98±0.11	4.55±0.06	9.28±0.05	6.70±0.90	SABb	3.0	Canyon	2	No
HCG45	b	2.30±0.02	1.29±0.01	1.92±0.01	2.85±1.02	Sa	0.8	Canyon	2	No
HCG45	c	0.33±0.02	0.21±0.01	0.41±0.01	2.73±1.13	Sc	4.9	Active	2	No
HCG45	d	0.52±0.02	0.32±0.02	0.60±0.04	4.39±2.52	S0	-2.0	Active	2	Yes
HCG46	b	2.59±0.07	1.43±0.04	1.47±0.03	4.09±1.27	S0	-1.9	Canyon	2	No
HCG46	c	2.09±0.07	1.10±0.04	0.38±0.09	3.63±2.64	E	-4.2	Quiescent	2	Yes
HCG46	d	2.51±0.06	1.40±0.03	1.46±0.02	3.62±3.88	S0	-1.6	Canyon	2	Yes
HCG47	a	15.38±0.10	8.48±0.05	34.55±0.21	69.94±0.36	SBab	2.4	Active	1	No
HCG47	c	1.19±0.03	0.70±0.02	2.35±0.11	8.76±1.11	Sc	6.0	Active	2	No
HCG47	d	0.76±0.06	0.41±0.02	0.87±0.05	3.98±2.30	Scd	6.6	Active	2	Yes

Table 1—Continued

Group	Galaxy	W1 mJy	W2 mJy	W3 mJy	W4 mJy	Morphology	De Vaucouleurs number*	WISE Class**	Photometry type***	Upper Limit****
HCG48	a	76.32±0.85	40.34±0.55	13.37±0.13	4.85±1.04	E	-3.9	Quiescent	2	No
HCG48	b	11.10±0.12	6.88±0.05	39.99±0.23	44.66±0.54	Sa	1.3	Active	1	No
HCG48	c	5.91±0.04	3.08±0.02	1.09±0.02	3.30±3.20	S0-a	-1.3	Quiescent	2	Yes
HCG48	d	1.51±0.05	0.80±0.02	0.24±0.02	3.72±4.56	E?	-2.0	Canyon	2	Yes
HCG49	a	0.66±0.03	0.39±0.02	2.29±0.10	15.12±1.15	Sc	4.6	Active	2	No
HCG49	b	0.63±0.02	0.51±0.02	4.52±0.15	31.55±1.43	Sd	8.0	Active	3	No
HCG49	c	0.28±0.01	0.19±0.01	0.75±0.11	3.36±0.91	I	10.0	Active	3	No
HCG49	d	0.16±0.01	0.09±0.00	0.26±0.01	2.09±0.78	E-S0	-3.3	Active	2	No
HCG50	c	0.43±0.01	0.31±0.01	0.34±0.33	2.07±0.86	S0	-2.0	Active	3	Yes
HCG51	a	13.49±0.30	6.75±0.13	1.89±0.13	1.86±0.89	E	-4.8	Quiescent	3	No
HCG51	b	8.37±0.10	4.62±0.04	10.34±0.07	7.53±1.12	SBbc	3.8	Canyon	2	No
HCG51	d	3.35±0.07	1.82±0.04	1.02±0.05	3.78±1.98	Sab	1.7	Quiescent	2	Yes
HCG51	e	8.42±0.09	4.42±0.05	2.30±0.05	3.18±1.08	E	-4.4	Quiescent	2	No
HCG51	g	0.64±0.06	0.35±0.03	0.12±0.00	2.74±2.89	E	-5.0	Canyon	2	Yes
HCG52	a	7.05±0.10	3.71±0.05	5.10±0.14	3.83±1.21	Sbc	3.9	Quiescent	2	No
HCG52	b	2.96±0.06	1.68±0.05	5.74±0.05	5.47±1.15	Sc	4.9	Active	2	No
HCG52	c	1.18±0.02	0.65±0.01	2.84±0.03	5.27±1.03	Sc	5.5	Active	2	No
HCG53	a	26.99±0.08	14.98±0.04	38.24±0.19	5.85±1.50	Sb	3.4	Quiescent	2	No
HCG53	b	10.58±0.09	5.59±0.04	3.08±0.07	2.87±1.06	S0-a	-0.9	Quiescent	2	No
HCG53	c	4.40±0.05	2.71±0.04	12.82±0.10	16.80±1.28	SBbc	4.2	Active	2	No
HCG54	a	0.99±0.03	0.58±0.02	1.29±0.14	9.23±1.07	S?	4.2	Active	3	No
HCG54	b	0.54±0.02	0.46±0.02	4.07±0.17	24.97±1.40	I	10.0	Active	3	No
HCG54	c	0.42±0.01	0.28±0.01	1.24±0.14	4.56±1.03	I	10.0	Active	3	No
HCG55	a	4.31±0.10	2.18±0.05	1.23±0.10	5.71±0.71	S0	-2.3	Quiescent	3	No
HCG55	b	2.56±0.06	1.32±0.03	0.67±0.09	2.60±1.77	E	-4.7	Quiescent	3	Yes
HCG55	c	3.66±0.08	2.20±0.05	7.04±0.16	9.37±0.71	SBa	1.3	Active	3	No
HCG56	a	4.96±0.03	2.99±0.05	9.32±0.08	11.12±1.03	SBbc	3.8	Active	2	No
HCG56	b	18.71±0.04	22.49±0.07	69.00±0.09	220.74±4.27	S0-a	0.0	Active	2	No
HCG56	c	5.10±0.12	2.72±0.06	1.60±0.11	2.70±1.98	S0	-1.9	Quiescent	3	Yes
HCG56	d	3.72±0.08	2.29±0.05	11.28±0.25	21.14±0.96	S0	-1.9	Active	3	No
HCG56	e	1.26±0.02	0.71±0.01	2.13±0.03	7.25±0.75	E-S0	-2.8	Active	2	No
HCG57	a	11.71±0.32	6.42±0.19	6.87±0.17	14.35±1.05	Sab	2.1	Canyon	2	No
HCG57	b	10.10±0.08	5.31±0.03	6.87±0.07	4.32±1.07	Sab	2.3	Quiescent	2	No
HCG57	d	2.83±0.15	1.64±0.10	5.47±0.41	20.09±1.14	SBb	3.4	Active	2	No
HCG57	e	7.05±0.05	3.73±0.03	3.72±0.10	3.83±1.14	S0	-1.9	Quiescent	2	No
HCG57	f	5.03±0.05	2.65±0.02	1.63±0.01	2.04±19.29	E-S0	-3.0	Quiescent	2	Yes
HCG57	h	0.80±0.01	0.45±0.00	1.05±0.05	7.66±4.68	S0-a	0.5	Active	2	Yes
HCG58	a	51.88±0.11	35.88±0.04	191.28±0.35	291.23±1.11	S0	-1.6	Active	1	No
HCG58	b	36.78±0.19	19.52±0.08	21.05±0.20	8.29±1.58	SBa	1.1	Quiescent	2	No
HCG58	c	19.49±0.10	10.20±0.03	5.35±0.05	4.35±1.49	S0-a	-0.1	Quiescent	2	No
HCG58	d	10.91±0.17	5.62±0.05	2.09±0.06	3.91±2.52	E	-4.7	Quiescent	2	Yes
HCG58	e	5.75±0.02	3.47±0.01	16.80±0.05	16.94±1.31	Sbc	3.6	Active	2	No
HCG59	a	11.28±0.04	9.20±0.03	63.08±0.16	474.46±7.38	S0-a	-0.7	Active	2	No
HCG59	b	2.66±0.06	1.37±0.02	0.64±0.06	4.88±1.78	E	-4.2	Canyon	2	No
HCG59	d	0.31±0.01	0.19±0.01	0.45±0.14	4.78±2.35	Scd	6.7	Active	3	No
HCG60	a	3.80±0.08	2.14±0.05	0.97±0.06	3.38±0.70	E	-3.8	Quiescent	2	No
HCG60	b	2.36±0.03	1.36±0.01	2.35±0.02	4.18±0.77	E-S0	-2.8	Canyon	2	No
HCG60	c	1.60±0.08	0.93±0.04	2.89±0.11	3.42±1.05	SBc	5.5	Active	2	No
HCG60	d	0.39±0.09	0.22±0.05	0.08±0.01	2.40±4.34	S0	-2.0	Active	2	Yes
HCG61	a	58.80±0.21	31.03±0.14	20.24±0.04	13.74±1.07	S0	-2.0	Quiescent	2	No
HCG61	c	48.01±0.15	32.55±0.05	164.48±0.09	357.72±1.55	Sb	3.2	Active	1	No
HCG61	d	12.32±0.06	6.72±0.03	2.52±0.06	3.65±1.97	S0-a	0.0	Quiescent	2	Yes
HCG62	a	18.66±0.53	9.77±0.31	3.23±0.08	5.16±1.13	S0	-1.6	Quiescent	2	No
HCG62	b	7.13±0.57	3.63±0.27	1.23±0.08	3.21±1.10	S0	-2.0	Quiescent	2	No
HCG62	c	7.71±0.24	4.12±0.10	1.61±0.03	4.56±2.32	S?	2.8	Quiescent	2	Yes
HCG62	d	3.47±0.01	1.85±0.02	0.83±0.02	7.07±4.27	E	-3.8	Canyon	2	Yes
HCG63	b	16.33±0.32	9.92±0.10	43.80±0.23	12.17±1.07	SBc	5.0	Canyon	2	No
HCG63	c	4.00±0.07	2.59±0.03	15.73±0.02	20.22±1.03	SBc	4.9	Active	2	No
HCG63	d	2.78±0.06	2.01±0.02	18.64±0.12	121.36±3.02	Sc	5.5	Active	2	No
HCG64	a	4.59±0.13	2.55±0.07	3.11±0.08	3.78±0.78	SBc	4.5	Quiescent	2	No
HCG64	b	1.82±0.03	1.12±0.02	2.65±0.04	6.56±1.19	Sc	5.8	Active	2	No
HCG64	d	0.64±0.02	0.36±0.02	0.36±0.11	3.12±1.64	S0	-2.0	Active	3	Yes
HCG65	a	5.17±0.27	2.72±0.16	0.96±0.05	3.61±1.77	E-S0	-3.2	Quiescent	2	Yes
HCG65	b	3.05±0.14	1.62±0.09	0.39±0.04	2.16±5.15	S0	-1.9	Quiescent	2	Yes
HCG65	c	3.63±0.15	1.93±0.09	0.63±0.09	3.13±2.21	E	-4.5	Quiescent	2	Yes
HCG65	d	0.99±0.05	0.54±0.03	0.59±0.32	2.23±1.02	E	-4.2	Canyon	3	Yes

Table 1—Continued

Group	Galaxy	W1 mJy	W2 mJy	W3 mJy	W4 mJy	Morphology	De Vaucouleurs number*	WISE Class**	Photometry type***	Upper Limit****
HCG65	e	3.76±0.09	1.78±0.05	0.87±0.11	1.97±0.84	E	-4.2	Quiescent	3	No
HCG66	a	2.01±0.11	1.06±0.06	0.38±0.05	3.00±2.70	E	-4.4	Quiescent	2	Yes
HCG66	b	0.39±0.13	0.24±0.07	0.54±0.02	4.00±0.85	S0	-2.0	Active	2	No
HCG66	c	0.59±0.03	0.32±0.02	0.14±0.02	2.45±3.63	S0	-2.0	Active	2	Yes
HCG67	a	33.35±0.46	17.38±0.26	5.41±0.03	5.39±0.86	S0	-2.4	Quiescent	2	No
HCG67	b	26.34±0.11	16.12±0.03	57.39±0.14	77.27±0.65	Sb	3.3	Active	1	No
HCG67	c	1.77±0.16	1.02±0.11	2.86±0.07	4.29±0.90	Sc	5.5	Active	2	No
HCG67	d	2.78±0.18	1.44±0.10	0.59±0.03	2.12±0.84	S0	-1.9	Quiescent	2	No
HCG68	a	170.88±1.35	87.51±0.89	33.39±0.21	18.98±1.04	S0	-2.0	Quiescent	2	No
HCG68	b	83.62±1.22	42.81±0.65	18.09±0.39	10.10±0.99	S0	-2.1	Quiescent	2	No
HCG68	c	97.64±4.18	56.04±2.31	188.48±0.40	182.43±3.84	Sbc	3.6	Active	2	No
HCG68	d	14.77±0.16	7.89±0.07	5.81±0.09	6.45±0.89	S0	-2.1	Quiescent	2	No
HCG68	e	9.09±0.06	4.78±0.03	1.67±0.02	1.94±9.52	S0-a	-0.2	Quiescent	2	Yes
HCG69	a	8.03±0.17	4.59±0.09	8.45±0.20	14.00±1.07	Sc	4.9	Canyon	3	No
HCG69	b	5.64±0.01	4.25±0.01	35.04±0.06	304.25±6.20	E	-4.2	Active	2	No
HCG69	c	2.42±0.08	1.24±0.03	0.34±0.06	1.88±8.95	E-S0	-2.8	Quiescent	2	Yes
HCG69	d	1.98±0.05	1.09±0.03	2.25±0.13	4.75±0.87	S0	-2.0	Active	3	No
HCG70	a	9.20±0.07	5.00±0.03	4.31±0.08	6.10±0.78	Sa	0.9	Quiescent	2	No
HCG70	b	9.96±0.04	5.74±0.02	12.43±0.05	29.99±1.13	SBa	0.7	Active	2	No
HCG70	c	3.01±0.01	1.62±0.02	4.88±0.03	3.90±0.80	Sbc	3.8	Canyon	2	No
HCG70	d	3.72±0.04	2.23±0.03	11.20±0.03	19.76±0.94	Sc	6.0	Active	2	No
HCG70	e	2.56±0.01	1.52±0.01	7.60±0.02	10.40±1.35	Sbc	3.9	Active	2	No
HCG70	f	0.42±0.01	0.24±0.00	1.21±0.03	3.19±1.53	Sb	3.0	Active	2	No
HCG70	g	3.54±0.03	2.07±0.02	6.00±0.07	11.18±0.74	Sa	1.0	Active	2	No
HCG71	a	14.96±0.12	8.34±0.05	23.35±0.17	14.86±1.02	Sc	5.8	Canyon	2	No
HCG71	b	6.10±0.02	4.04±0.02	17.30±0.02	56.51±1.60	Sb	3.0	Active	2	No
HCG71	c	1.32±0.02	0.76±0.00	3.51±0.02	4.79±0.72	SBc	4.9	Active	2	No
HCG72	a	4.72±0.04	2.53±0.01	1.61±0.04	2.29±0.73	S0-a	-0.5	Quiescent	2	No
HCG72	b	1.60±0.08	0.86±0.04	0.30±0.01	2.68±1.55	S0	-2.0	Quiescent	2	Yes
HCG72	c	3.42±0.07	1.83±0.04	0.55±0.09	2.45±2.52	E-S0	-3.3	Quiescent	2	Yes
HCG72	d	1.85±0.09	0.96±0.04	0.38±0.03	3.06±1.63	S0	-1.9	Quiescent	2	Yes
HCG72	f	0.42±0.01	0.23±0.01	0.31±0.10	1.76±16.79	S0	-2.0	Active	3	Yes
HCG73	b	4.14±0.04	2.81±0.01	15.70±0.04	38.46±1.52	Sm	8.9	Active	2	No
HCG73	d	0.93±0.02	0.62±0.01	1.59±0.03	3.81±2.56	Sb	3.0	Active	2	Yes
HCG74	a	7.88±0.26	4.19±0.15	1.32±0.07	2.13±0.66	E	-4.4	Quiescent	2	No
HCG74	b	1.75±0.17	0.93±0.09	0.24±0.02	2.38±1.87	E	-4.2	Quiescent	2	Yes
HCG74	d	2.48±0.03	1.28±0.01	0.64±0.02	4.16±2.35	E	-5.0	Canyon	2	Yes
HCG75	a	11.08±0.25	5.54±0.12	2.28±0.11	3.51±0.74	S?	2.2	Quiescent	3	No
HCG75	c	1.77±0.02	0.96±0.01	0.84±0.01	2.48±0.69	S0	-2.0	Canyon	2	No
HCG75	d	2.32±0.03	1.48±0.03	7.58±0.07	9.38±1.08	Sd	8.0	Active	2	No
HCG76	a	7.45±0.03	4.07±0.03	2.21±0.03	2.63±2.21	Sb	2.6	Quiescent	2	Yes
HCG76	b	2.73±0.13	1.46±0.06	0.49±0.06	3.09±1.61	E	-3.9	Quiescent	2	Yes
HCG76	c	9.24±0.08	4.93±0.04	1.52±0.06	1.86±0.70	E	-4.4	Quiescent	2	No
HCG76	d	4.25±0.05	2.28±0.04	0.78±0.07	3.15±1.47	E	-4.4	Quiescent	2	No
HCG76	e	0.83±0.03	0.43±0.01	0.21±0.00	2.52±2.68	S0	-2.0	Canyon	2	Yes
HCG76	f	1.93±0.05	1.09±0.03	0.94±0.09	1.84±17.26	Sc	6.0	Quiescent	3	Yes
HCG79	a	12.62±0.26	7.50±0.14	17.08±0.31	25.00±1.25	S0-a	0.3	Active	3	No
HCG79	b	13.57±0.27	7.79±0.15	11.93±0.27	28.78±1.60	S0	-1.6	Active	3	No
HCG79	c	2.21±0.07	1.21±0.04	0.36±0.15	3.96±1.47	S0-a	-1.5	Quiescent	3	No
HCG79	d	0.72±0.02	0.40±0.01	1.37±0.14	5.72±1.23	SBc	5.2	Active	3	No
HCG80	a	10.81±0.17	8.59±0.02	51.54±0.17	122.78±2.68	Sc	6.5	Active	2	No
HCG80	b	2.99±0.05	1.67±0.02	1.27±0.06	3.30±1.81	Sa	1.0	Quiescent	2	Yes
HCG80	c	1.82±0.04	1.25±0.01	7.30±0.05	15.43±0.76	Sm	8.9	Active	2	No
HCG80	d	0.64±0.01	0.39±0.01	1.37±0.01	2.65±0.53	I	10.0	Active	2	No
HCG81	a	2.90±0.04	2.17±0.02	18.87±0.13	28.62±2.14	Sb	2.8	Active	2	No
HCG81	b	1.31±0.07	0.71±0.03	0.29±0.02	2.89±3.28	S0-a	-1.1	Canyon	2	Yes
HCG81	c	2.83±0.07	1.57±0.04	2.37±0.14	3.07±1.14	S0	-2.0	Canyon	3	No
HCG82	a	11.84±0.19	6.23±0.11	2.31±0.02	2.32±0.83	S0	-2.2	Quiescent	2	No
HCG82	b	8.99±0.13	4.81±0.07	4.06±0.04	5.81±0.96	S0	-1.7	Quiescent	2	No
HCG82	c	5.77±0.07	4.19±0.04	29.01±0.19	90.47±2.65	Sd	7.8	Active	2	No
HCG82	d	0.72±0.04	0.39±0.02	0.14±0.02	5.85±4.51	S0-a	0.0	Active	2	Yes
HCG83	a	2.98±0.02	1.58±0.02	0.76±0.02	2.23±6.76	E	-4.2	Quiescent	2	Yes
HCG83	b	2.97±0.07	1.47±0.04	0.59±0.13	3.62±2.09	E	-4.2	Quiescent	3	Yes
HCG83	c	0.72±0.01	0.48±0.01	3.50±0.02	7.64±1.78	Scd	7.0	Active	2	No
HCG83	d	0.40±0.02	0.28±0.02	0.75±0.14	3.64±2.43	E	-3.5	Active	3	Yes
HCG84	a	2.99±0.10	1.54±0.06	0.56±0.02	2.55±1.33	E	-3.9	Quiescent	2	Yes

Table 1—Continued

Group	Galaxy	W1 mJy	W2 mJy	W3 mJy	W4 mJy	Morphology De Vaucouleurs number*	WISE Class**	Photometry type***	Upper Limit****
HCG84	c	0.86±0.06	0.45±0.03	0.19±0.02	1.44±3.26	Sa	1.0	Canyon	2	Yes
HCG85	a	10.38±0.15	5.55±0.09	2.18±0.08	1.64±0.59	E	-4.4	Quiescent	2	No
HCG85	b	9.63±0.18	5.36±0.09	1.56±0.05	1.68±0.65	E	-4.4	Quiescent	2	No
HCG85	c	1.50±0.03	0.84±0.02	0.61±0.01	1.44±0.60	E-S0	-2.8	Quiescent	2	No
HCG85	d	0.17±0.01	0.10±0.01	0.04±0.00	1.89±2.49	E	-5.0	Active	2	Yes
HCG86	a	38.40±0.34	19.98±0.18	6.39±0.03	3.20±0.95	E-S0	-3.2	Quiescent	2	No
HCG86	b	20.50±0.14	11.00±0.09	7.44±0.18	8.19±1.38	E	-3.9	Quiescent	2	No
HCG86	c	12.56±0.07	6.89±0.04	5.92±0.04	10.68±1.16	S0-a	-1.2	Quiescent	2	No
HCG86	d	6.29±0.13	3.39±0.06	1.13±0.02	3.08±9.85	S0-a	-1.3	Quiescent	2	Yes
HCG87	a	17.57±0.24	9.89±0.11	11.04±0.07	6.13±3.05	S0-a	-1.1	Quiescent	2	Yes
HCG87	b	7.00±0.09	3.74±0.06	2.02±0.03	2.63±1.12	E-S0	-2.6	Quiescent	2	No
HCG87	c	2.37±0.06	1.39±0.03	5.82±0.05	7.90±1.17	Sc	4.8	Active	2	No
HCG88	a	30.67±0.19	16.76±0.12	37.87±0.15	24.12±1.79	Sb	2.7	Canyon	2	No
HCG88	b	24.08±0.15	12.42±0.11	27.14±0.08	8.26±1.58	Sa	1.3	Quiescent	2	No
HCG88	c	7.25±0.07	4.11±0.03	22.00±0.10	21.24±1.55	SABb	4.1	Active	2	No
HCG88	d	4.01±0.06	2.28±0.03	9.55±0.04	10.89±1.47	Sc	4.9	Active	2	No
HCG89	a	4.32±0.05	2.42±0.03	11.38±0.25	11.80±1.30	Sc	4.7	Active	2	No
HCG89	b	1.82±0.02	1.15±0.03	7.70±0.03	21.49±1.33	Sc	5.5	Active	2	No
HCG89	c	1.41±0.02	0.76±0.02	3.77±0.08	6.55±4.03	Sc	6.4	Active	2	Yes
HCG89	d	0.09±0.01	0.05±0.01	0.20±0.02	3.55±1.29	Sm	9.0	Active	2	No
HCG90	a	186.55±0.45	178.70±0.41	291.51±0.61	551.20±1.29	Sa	0.6	Active	1	No
HCG90	b	56.87±1.18	30.20±0.57	9.31±0.26	18.09±1.39	E	-4.8	Quiescent	3	No
HCG90	c	58.91±0.75	31.26±0.45	8.96±0.38	3.17±1.09	E	-4.3	Quiescent	2	No
HCG90	d	29.74±0.95	18.39±0.56	50.91±0.55	135.22±2.01	Sb	2.5	Active	1	No
HCG91	a	50.17±0.53	41.79±0.26	150.72±0.48	361.61±0.56	Sbc	4.5	Active	1	No
HCG91	b	14.94±0.08	10.25±0.05	53.96±0.25	157.04±0.68	Sc	4.8	Active	1	No
HCG91	c	6.15±0.05	3.83±0.04	19.24±0.10	20.41±1.50	Sc	4.9	Active	2	No
HCG91	d	2.73±0.13	1.51±0.08	0.62±0.15	3.22±10.17	S0	-1.9	Quiescent	2	Yes
HCG92	b	5.94±0.22	3.13±0.12	1.03±0.05	2.74±0.95	SBbc	4.1	Quiescent	2	No
HCG92	c	17.01±0.24	18.63±0.16	63.60±0.44	209.18±4.38	Sbc	4.0	Active	2	No
HCG92	d	8.25±0.21	4.24±0.13	1.33±0.13	2.21±0.94	E	-4.8	Quiescent	2	No
HCG92	e	4.72±0.31	2.46±0.17	0.80±0.05	3.89±2.02	E	-4.6	Quiescent	2	Yes
HCG93	a	67.94±0.51	35.07±0.23	17.70±0.07	7.87±1.21	E-S0	-3.1	Quiescent	2	No
HCG93	b	32.10±0.24	18.37±1.03	91.21±0.15	143.46±0.21	Sc	5.9	Active	1	No
HCG93	c	25.17±0.20	13.39±0.07	14.06±0.04	12.71±1.13	Sa	0.9	Quiescent	2	No
HCG94	a	8.73±0.33	4.55±0.18	1.26±0.03	2.46±1.03	E	-4.9	Quiescent	2	No
HCG94	b	4.61±0.26	2.39±0.14	0.84±0.04	3.75±2.75	S0	-2.2	Quiescent	2	Yes
HCG94	d	2.68±0.42	1.35±0.24	0.32±0.06	2.93±4.94	E-S0	-2.8	Quiescent	2	Yes
HCG94	e	0.74±0.03	0.49±0.03	1.86±0.05	4.86±1.56	Sc	6.1	Active	2	No
HCG94	f	0.39±0.03	0.20±0.01	0.21±0.04	4.12±2.35	E-S0	-2.8	Active	2	Yes
HCG94	g	0.16±0.01	0.09±0.01	0.11±0.01	3.78±2.59	E-S0	-2.8	Active	2	Yes
HCG95	a	4.76±0.15	2.52±0.08	1.72±0.06	4.99±2.38	E	-4.4	Quiescent	2	No
HCG95	b	6.05±0.06	4.04±0.03	23.43±0.13	38.38±1.48	Sc	5.7	Active	2	No
HCG95	c	1.98±0.08	1.23±0.05	4.53±0.06	20.62±1.19	Sm	9.0	Active	2	No
HCG95	d	2.94±0.04	1.71±0.04	4.31±0.09	4.90±0.98	Sbc	4.4	Active	2	No
HCG96	a	57.22±0.28	84.84±0.26	376.58±1.05	1545.75±28.36	SBbc	3.8	Active	2	No
HCG96	b	10.84±0.11	5.63±0.06	2.15±0.03	4.31±5.12	E-S0	-3.1	Quiescent	2	Yes
HCG96	c	3.13±0.07	1.94±0.04	9.16±0.24	4.49±0.90	S?	5.5	Active	1	No
HCG96	d	0.60±0.02	0.36±0.01	2.72±0.05	11.44±1.23	I	10.0	Active	2	No
HCG97	a	13.87±0.31	7.15±0.13	2.29±0.15	2.82±4.49	E-S0	-3.2	Quiescent	2	Yes
HCG97	b	7.38±0.06	4.19±0.04	12.28±0.03	8.80±1.17	Sc	5.1	Canyon	2	No
HCG97	c	8.05±0.07	4.21±0.04	1.28±0.03	2.69±6.46	Sa	0.6	Quiescent	2	Yes
HCG97	e	1.14±0.07	0.60±0.03	0.16±0.04	2.56±6.16	S0	-1.6	Canyon	2	Yes
HCG98	a	20.93±0.26	11.04±0.13	3.62±0.01	3.98±1.11	S0	-1.8	Quiescent	2	No
HCG98	b	4.69±0.14	2.50±0.08	0.87±0.04	4.26±2.01	E-S0	-2.9	Quiescent	2	No
HCG98	c	1.99±0.03	1.03±0.02	0.34±0.01	3.63±11.46	E	-4.2	Quiescent	2	Yes
HCG99	a	2.96±0.30	1.55±0.17	0.76±0.05	4.11±1.07	Sab	1.9	Quiescent	2	No
HCG99	b	12.74±0.22	6.72±0.10	2.51±0.09	2.44±5.74	E	-4.1	Quiescent	2	Yes
HCG99	c	3.04±0.20	1.63±0.11	1.62±0.15	2.78±1.12	SBa	1.5	Quiescent	2	No
HCG99	d	0.82±0.02	0.44±0.01	0.23±0.02	2.14±0.95	S0-a	-0.2	Canyon	2	No
HCG99	e	0.44±0.02	0.24±0.01	0.15±0.01	3.42±1.93	S0	-2.0	Active	2	Yes
HCG100	a	28.39±0.15	16.79±0.10	52.43±0.11	139.56±0.63	S0-a	0.1	Active	1	No
HCG100	b	3.67±0.02	2.28±0.03	10.78±0.08	26.58±1.44	Sm	9.0	Active	2	No
HCG100	c	1.71±0.03	1.02±0.01	3.29±0.04	11.94±1.49	SBc	4.9	Active	2	No
HCG100	d	0.47±0.04	0.29±0.03	0.79±0.04	3.81±2.88	Sc	5.5	Active	2	Yes
RSCG01	NGC0070	6.94±0.35	3.69±0.20	2.39±0.45	10.66±1.13	Sbc	4.4	Canyon	2	No

Table 1—Continued

Group	Galaxy	W1 mJy	W2 mJy	W3 mJy	W4 mJy	Morphology De	Vaucouleurs number*	WISE Class**	Photometry type***	Upper Limit****
RSCG01	NGC0068	16.60±0.50	8.68±0.29	4.98±0.24	5.54±1.26	E-S0	-3.1	Quiescent	2	No
RSCG01	NGC0072	15.71±0.12	8.29±0.04	6.90±0.03	5.66±1.03	Sab	1.6	Quiescent	2	No
RSCG01	NGC0072A	5.63±0.04	2.90±0.03	1.06±0.03	7.59±3.67	E	-5.0	Quiescent	2	No
RSCG02	UGC00335NED01	4.11±0.09	2.20±0.05	2.84±0.05	4.01±1.69	E	-4.8	Canyon	2	No
RSCG02	UGC00335NED02	7.63±0.17	3.98±0.10	1.61±0.05	4.36±5.26	S0	-2.0	Quiescent	2	Yes
RSCG02	UGC00331	7.34±0.06	3.73±0.04	1.49±0.07	4.56±1.41	Sa	1.0	Quiescent	2	No
RSCG04	NGC0232	37.01±0.09	28.10±0.06	209.73±0.31	818.41±14.50	SBa	1.1	Active	2	No
RSCG04	NGC0235B	4.07±0.09	2.19±0.05	2.06±0.15	33.62±1.49	S0	-2.0	Active	3	No
RSCG04	NGC0232E	27.57±0.59	28.46±0.53	109.57±1.54	399.42±7.69	S0	-2.2	Active	3	No
RSCG05	NGC0383	52.71±0.81	28.41±0.41	19.97±0.08	22.53±1.18	E-S0	-2.9	Quiescent	2	No
RSCG05	NGC0382	10.80±0.52	5.81±0.26	4.34±0.13	9.53±0.99	E	-4.8	Quiescent	2	No
RSCG05	NGC0386	7.51±0.05	3.93±0.02	1.41±0.02	1.83±0.76	E	-5.0	Quiescent	2	No
RSCG05	NGC0385	21.25±0.29	11.27±0.12	4.48±0.05	5.41±0.83	E	-3.7	Quiescent	2	No
RSCG05	NGC0384	22.39±0.17	11.80±0.07	6.53±0.02	7.51±0.80	E	-4.2	Quiescent	2	No
RSCG06	UGC00816	13.18±0.24	8.83±0.12	62.60±0.22	84.08±0.46	SABc	4.6	Active	1	No
RSCG06	UGC00813	11.30±0.08	7.40±0.07	44.93±0.19	78.73±2.14	-	-	Active	2	No
RSCG06	CGCG551-011	11.12±0.10	7.57±0.06	22.55±0.09	61.22±1.83	Sab	2.1	Active	2	No
RSCG07	NGC0501	8.12±0.03	4.15±0.02	1.33±0.02	1.93±3.77	E	-5.0	Quiescent	2	Yes
RSCG07	NGC0499	81.12±0.49	42.23±0.31	13.44±0.24	5.55±0.76	E-S0	-2.9	Quiescent	2	No
RSCG07	NGC0495	22.70±0.19	11.81±0.07	4.06±0.04	2.71±0.88	S0-a	0.2	Quiescent	2	No
RSCG08	NGC0503	6.51±0.05	3.35±0.03	0.92±0.04	2.89±1.99	S0	-1.6	Quiescent	2	Yes
RSCG08	NGC0508	25.16±0.68	13.37±0.31	15.15±0.08	17.87±1.19	E	-4.9	Quiescent	2	No
RSCG08	NGC0507	78.40±1.85	41.29±1.01	13.36±0.05	5.46±0.91	E-S0	-3.3	Quiescent	2	No
RSCG08	NGC0504	21.41±0.12	11.25±0.09	3.42±0.09	2.80±0.78	S0	-2.0	Quiescent	2	No
RSCG09	IC1698	13.36±0.10	7.22±0.06	8.24±0.09	5.43±0.84	S0	-1.8	Quiescent	2	No
RSCG09	IC0107	18.14±0.21	9.67±0.10	4.22±0.11	3.69±0.88	Sc	5.8	Quiescent	2	No
RSCG09	UGC00978	5.31±0.28	3.09±0.18	11.68±0.06	8.08±0.87	Sc	5.8	Active	2	No
RSCG10	UGC00996	10.34±0.05	5.50±0.05	2.21±0.04	2.37±0.91	S0-a	-0.3	Quiescent	2	No
RSCG10	NGC0538	11.82±0.35	6.20±0.17	1.95±0.03	3.87±2.07	SBab	1.6	Quiescent	2	Yes
RSCG10	UGC00984	8.03±0.05	4.22±0.03	1.49±0.01	3.25±1.84	S0	-1.9	Quiescent	2	Yes
RSCG13	IC1724	22.78±0.09	12.13±0.06	6.40±0.02	5.48±0.95	S0-a	-1.1	Quiescent	2	No
RSCG13	ESO353-G036	19.75±0.04	14.86±0.04	118.36±0.22	251.71±1.19	S0	-1.6	Active	1	No
RSCG13	IC1722	5.24±0.01	3.29±0.02	13.47±0.10	11.92±1.14	SABb	4.2	Active	2	No
RSCG14	NGC678	111.21±0.51	60.20±0.30	58.55±0.20	39.84±1.51	SBb	3.0	Quiescent	2	No
RSCG14	NGC680	89.30±0.43	47.15±0.28	17.69±0.19	8.50±0.91	E	-4.1	Quiescent	2	No
RSCG14	IC1730	4.28±0.10	2.29±0.05	1.42±0.06	2.99±0.79	S?	1.0	Quiescent	2	No
RSCG15	NGC704	12.85±0.17	6.79±0.09	2.12±0.05	4.07±2.62	E-S0	-3.5	Quiescent	2	Yes
RSCG15	NGC705	15.70±0.37	8.51±0.18	3.70±0.12	3.08±1.00	S0-a	-0.1	Quiescent	2	No
RSCG15	NGC708	32.26±0.80	17.05±0.43	7.20±0.18	3.69±1.04	E	-4.9	Quiescent	2	No
RSCG15	NGC703	23.06±0.20	12.74±0.10	11.24±0.06	14.57±0.99	E-S0	-3.1	Quiescent	2	No
RSCG16	MCG+06-05-047	9.51±0.11	5.50±0.03	14.09±0.12	30.31±1.17	Sb	3.0	Active	2	No
RSCG16	MRK2	19.10±0.09	14.21±0.07	134.37±0.17	767.74±13.89	SBa	0.6	Active	2	No
RSCG16	MCG+06-05-048	3.69±0.09	2.29±0.05	11.17±0.07	11.76±0.81	Sb	3.1	Active	2	No
RSCG17	ARK066	8.32±0.14	4.26±0.06	1.89±0.06	2.55±3.57	E	-5.0	Quiescent	2	Yes
RSCG17	NGC742	10.35±0.46	5.53±0.24	3.54±0.07	9.87±1.02	E-S0	-3.3	Quiescent	2	No
RSCG17	NGC741	62.40±1.13	32.61±0.64	10.30±0.20	5.59±0.90	E	-4.8	Quiescent	2	No
RSCG18	NGC740	12.12±0.15	6.84±0.13	21.79±0.21	21.84±1.57	SBb	3.2	Active	2	No
RSCG18	NGC738	5.86±0.05	3.02±0.05	1.35±0.07	4.13±1.77	S0	-2.0	Quiescent	2	No
RSCG18	NGC736	40.58±0.64	21.07±0.34	6.71±0.11	3.56±1.31	E	-4.0	Quiescent	2	No
RSCG22	NGC1332	373.90±1.78	197.24±1.12	70.69±0.11	32.14±1.30	E-S0	-2.9	Quiescent	2	No
RSCG22	NGC1331	12.32±0.16	6.72±0.10	2.22±0.03	1.97±0.67	E	-4.7	Quiescent	2	No
RSCG22	2MASXJ03263135-2113003	7.68±0.05	4.08±0.03	1.27±0.05	2.44±0.71	E	-5.0	Quiescent	2	No
RSCG23	ESO358-25	10.19±0.12	5.97±0.06	16.71±0.03	21.47±1.11	E-S0	-2.6	Active	2	No
RSCG23	ESO358-20	3.62±0.06	2.04±0.05	5.27±0.08	2.97±0.72	SBm	9.3	Canyon	2	No
RSCG23	ESO358-22	12.14±0.19	6.55±0.10	2.02±0.10	1.75±1.74	S0	-2.0	Quiescent	2	Yes
RSCG24	NGC1386	184.27±0.43	152.61±0.26	454.70±0.22	1266.13±19.48	S0-a	-0.7	Active	2	No
RSCG24	NGC1389	103.63±0.48	55.79±0.18	17.58±0.08	6.79±0.65	E-S0	-2.8	Quiescent	2	No
RSCG24	NGC1387	323.77±0.71	174.95±0.43	111.22±0.42	100.86±0.79	E-S0	-2.8	Quiescent	1	No
RSCG24	NGC1379	161.23±0.57	87.64±0.28	25.08±0.07	4.24±0.58	E	-4.8	Quiescent	2	No
RSCG24	NGC1381	126.57±0.21	67.70±0.11	20.60±0.06	6.18±0.59	S0	-2.1	Quiescent	2	No
RSCG24	NGC1375	34.21±0.27	18.80±0.16	6.25±0.05	4.09±0.59	S0	-2.2	Quiescent	2	No
RSCG24	NGC1374	140.32±0.93	75.37±0.57	21.26±0.14	7.27±0.63	E	-4.5	Quiescent	2	No
RSCG24	MCG-06-09-008	5.56±0.06	2.98±0.03	1.07±0.02	1.54±3.04	E-S0	-2.8	Quiescent	2	Yes
RSCG24	NGC1380	510.84±1.37	277.67±0.65	102.59±0.97	48.03±1.49	S0	-2.3	Quiescent	2	No
RSCG24	NGC1399	839.01±8.57	447.34±3.91	116.52±0.58	24.43±0.99	E	-4.6	Quiescent	2	No
RSCG24	NGC1404	353.42±3.24	186.41±1.81	58.87±0.30	21.54±0.95	E	-4.8	Quiescent	2	No

Table 1—Continued

Group	Galaxy	W1 mJy	W2 mJy	W3 mJy	W4 mJy	Morphology	De Vaucouleurs number*	WISE Class**	Photometry type***	Upper Limit****
RSCG24	NGC1373	13.31±0.08	7.18±0.04	2.05±0.04	2.11±1.31	E	-3.6	Quiescent	2	Yes
RSCG24	NGC1396	2.61±0.04	1.40±0.03	0.47±0.03	1.42±3.53	E-S0	-3.1	Quiescent	2	Yes
RSCG25	NGC1407	585.98±5.65	312.58±2.91	94.44±0.45	15.57±1.07	E	-4.5	Quiescent	2	No
RSCG25	NGC1400	225.61±0.90	121.76±0.49	82.85±0.17	65.75±0.55	E	-3.7	Quiescent	1	No
RSCG25	IC343	15.44±0.17	8.26±0.10	3.31±0.07	2.06±0.88	S0-a	-1.1	Quiescent	2	No
RSCG26	NGC1532	597.30±3.74	348.49±2.05	765.37±0.34	1041.61±2.36	SBb	3.1	Active	1	No
RSCG26	NGC1531	37.41±0.63	21.78±0.41	34.61±1.37	35.14±1.46	E-S0	-2.5	Canyon	2	No
RSCG27	ESO-LV420-0141	2.54±0.06	2.30±0.05	30.63±0.47	280.71±5.44	Sa	1.0	Active	3	No
RSCG27	ESO-LV420-0140	2.69±0.07	2.37±0.06	32.60±0.52	194.99±4.44	Sa	1.0	Active	3	No
RSCG27	ESO-LV420-0142	2.29±0.05	1.38±0.04	8.69±0.19	32.47±1.45	Sa	1.0	Active	3	No
RSCG28	NGC2738	29.05±0.13	19.02±0.04	144.58±0.50	243.76±0.73	Sbc	3.9	Active	1	No
RSCG28	MCG+04-22-007	1.47±0.03	0.83±0.02	1.84±0.03	2.33±0.95	Sbc	3.8	Canyon	2	No
RSCG28	NGC2737	17.44±0.07	9.06±0.02	3.38±0.04	2.94±1.37	Sab	2.0	Quiescent	2	No
RSCG29	IC2441NED01	1.37±0.05	0.71±0.02	0.21±0.08	3.89±3.03	E	-5.0	Canyon	2	Yes
RSCG29	IC2441NED02	1.49±0.15	0.81±0.08	1.82±0.07	6.58±1.31	-	-	Active	2	No
RSCG29	IC2442	6.44±0.09	3.79±0.08	17.69±0.11	22.41±1.41	-	-	Active	2	No
RSCG29	2MASXJ09100936+2250187	0.74±0.02	0.43±0.01	2.59±0.07	3.99±1.70	-	-	Active	2	No
RSCG30	NGC2780	15.72±0.07	8.77±0.04	28.84±0.12	24.41±1.45	Sb	3.0	Active	2	No
RSCG30	NGC2778	32.43±0.24	16.60±0.11	5.13±0.07	3.04±1.25	E	-4.8	Quiescent	2	No
RSCG30	NGC2779	2.42±0.05	1.26±0.03	3.22±0.01	4.18±1.18	S0-a	0.0	Active	2	No
RSCG31	NGC2799	9.42±0.19	5.58±0.16	23.66±0.45	32.34±1.80	SBm	8.8	Active	2	No
RSCG31	NGC2798	85.80±0.35	60.74±0.16	522.24±0.46	2327.22±37.52	SBa	1.1	Active	2	No
RSCG31	UGC4904	3.55±0.02	1.95±0.01	4.59±0.05	7.74±0.96	SBbc	4.3	Active	2	No
RSCG32	NGC2830	14.10±0.61	8.65±0.25	24.25±0.05	32.34±1.38	S0-a	-0.7	Active	2	No
RSCG32	NGC2831	3.00±0.20	1.63±0.11	1.77±0.06	7.00±1.20	E	-4.7	Canyon	2	No
RSCG32	NGC2832	24.53±0.70	12.55±0.36	4.43±0.10	4.31±1.02	E	-4.3	Quiescent	2	No
RSCG33	UGC5093	9.25±0.04	5.17±0.04	19.44±0.03	13.94±1.46	Sbc	3.8	Active	2	No
RSCG33	NGC2914	22.11±0.15	11.48±0.07	4.57±0.08	6.72±1.29	SBab	2.1	Quiescent	2	No
RSCG33	NGC2911	63.44±0.85	33.22±0.42	23.15±0.09	13.84±1.15	S0	-2.0	Quiescent	2	No
RSCG34	NGC2964	222.54±0.53	203.51±0.40	616.45±0.95	1363.46±4.26	Sbc	4.1	Active	1	No
RSCG34	NGC2968	100.88±0.84	52.57±0.38	16.76±0.24	5.36±1.11	Sa	1.2	Quiescent	2	No
RSCG34	NGC2970	6.80±0.13	3.66±0.07	1.89±0.02	3.64±2.11	E	-4.6	Quiescent	2	Yes
RSCG36	NGC3389	55.34±0.18	34.02±0.08	173.82±0.21	316.47±0.73	Sc	5.3	Active	1	No
RSCG36	NGC3384	459.42±1.75	241.53±0.86	75.39±0.46	24.48±1.49	E-S0	-2.7	Quiescent	2	No
RSCG36	NGC3379	811.86±5.04	424.74±2.59	117.92±1.14	27.53±1.20	E	-4.8	Quiescent	2	No
RSCG37	NGC3377	218.53±1.97	116.18±0.95	34.53±0.32	12.79±1.11	E	-4.8	Quiescent	2	No
RSCG38	NGC3430	88.19±0.34	52.10±0.14	241.11±0.38	347.39±2.07	Sc	5.1	Active	1	No
RSCG38	NGC3424	87.49±0.29	56.92±0.18	321.16±0.39	668.14±1.64	SBb	3.1	Active	1	No
RSCG38	NGC3413	17.29±0.09	9.81±0.03	24.64±0.06	65.10±0.29	S0	-1.5	Active	1	No
RSCG39	UGC6035	2.44±0.06	1.28±0.03	1.48±0.05	3.91±2.17	IB	9.9	Canyon	2	Yes
RSCG39	CGCG095-070	2.05±0.02	1.13±0.01	3.78±0.02	6.37±1.13	S?	5.0	Active	2	No
RSCG39	NGC3454	22.35±0.12	13.31±0.14	44.41±0.21	65.61±1.38	Sbc	5.4	Active	1	No
RSCG39	NGC3455	20.82±0.21	11.87±0.08	53.84±0.13	72.08±0.58	SABb	3.1	Active	1	No
RSCG40	NGC3608	162.50±0.91	84.54±0.54	27.66±0.09	7.67±1.08	E	-4.8	Quiescent	2	No
RSCG40	NGC3607	426.86±3.43	223.85±1.80	123.44±0.22	79.53±0.34	E-S0	-3.2	Quiescent	1	No
RSCG40	NGC3605	31.92±0.28	16.48±0.09	5.26±0.03	5.53±2.90	E	-4.5	Quiescent	2	Yes
RSCG40	UGC6296	19.84±0.10	11.31±0.03	39.26±0.06	23.09±1.34	Sd	8.0	Canyon	2	No
RSCG40	NGC3599	44.20±0.66	22.93±0.30	19.17±0.11	33.40±1.76	S0	-2.0	Quiescent	2	No
RSCG41	NGC3691	18.23±0.06	10.02±0.05	36.06±0.23	6.80±1.25	SBb	3.0	Quiescent	2	No
RSCG41	NGC3686	134.56±0.56	79.48±0.30	335.98±0.44	513.81±1.52	SBbc	4.1	Active	1	No
RSCG41	NGC3684	66.60±0.35	39.57±0.07	192.23±0.55	244.73±1.13	Sbc	4.0	Active	1	No
RSCG41	NGC3681	72.67±0.24	38.76±0.14	64.36±0.25	11.18±1.17	Sbc	4.0	Quiescent	2	No
RSCG42	MRK181	12.05±0.07	8.54±0.02	72.38±0.08	195.05±0.65	SBd	8.4	Active	1	No
RSCG42	MCG+03-30-021	8.06±0.08	4.69±0.05	22.03±0.08	21.05±1.26	Sc	5.8	Active	2	No
RSCG44	NGC3837	20.60±0.19	10.77±0.10	7.20±0.03	10.59±1.33	E	-4.9	Quiescent	2	No
RSCG44	UGC6697	17.17±0.02	10.85±0.03	51.99±0.24	87.48±0.32	Sm	9.4	Active	1	No
RSCG44	NGC3842	45.91±0.70	23.31±0.37	7.01±0.01	4.33±3.54	E	-4.9	Quiescent	2	Yes
RSCG44	NGC3841	8.77±0.19	4.45±0.09	1.61±0.03	2.60±4.30	E-S0	-3.3	Quiescent	2	Yes
RSCG44	NGC3845	7.80±0.05	4.04±0.03	1.44±0.01	3.92±2.09	S0-a	-0.5	Quiescent	2	Yes
RSCG45	MCG+03-30-079	3.56±0.06	1.88±0.04	0.71±0.02	2.55±4.10	S0	-2.5	Quiescent	2	Yes
RSCG45	MCG+03-30-078	5.70±0.06	2.89±0.03	1.11±0.06	3.14±2.39	S0-a	-1.0	Quiescent	2	Yes
RSCG45	MCG+03-30-076	9.40±0.11	4.83±0.06	2.00±0.02	3.40±3.32	Sab	1.5	Quiescent	2	Yes
RSCG47	NGC3995	23.82±0.28	14.88±0.41	99.83±1.34	271.95±1.55	SABm	8.8	Active	1	No
RSCG47	NGC3994	46.91±0.19	30.02±0.11	186.40±0.38	342.92±1.64	Sc	4.9	Active	1	No
RSCG47	LEDA200277	4.86±0.11	2.97±0.06	23.15±0.39	130.48±2.98	-	-	Active	3	No
RSCG48	NGC4117	20.78±0.14	11.25±0.06	10.80±0.16	30.52±1.32	S0	-2.1	Canyon	2	No

Table 1—Continued

Group	Galaxy	W1 mJy	W2 mJy	W3 mJy	W4 mJy	Morphology	De Vaucouleurs number*	WISE Class**	Photometry type***	Upper Limit****
RSCG48	NGC4111	264.48±0.80	142.46±0.43	66.94±0.15	67.42±1.86	S0-a	-1.3	Quiescent	2	No
RSCG48	UGC7089	8.21±0.14	4.20±0.12	7.05±0.12	2.70±1.00	Sd	7.9	Quiescent	2	No
RSCG50	NGC4206	49.19±0.18	26.67±0.03	69.66±0.15	20.18±1.23	Sbc	4.0	Quiescent	2	No
RSCG50	IC3066	1.54±0.02	0.85±0.01	1.52±0.02	4.72±3.93	Sbc	4.2	Active	2	Yes
RSCG51	NGC4278	378.23±1.92	198.67±1.03	80.65±0.19	32.32±1.90	E	-4.8	Quiescent	2	No
RSCG51	NGC4283	60.46±0.32	31.26±0.16	11.00±0.12	5.39±1.28	E	-4.8	Quiescent	2	No
RSCG51	NGC4286	8.40±0.20	4.43±0.09	10.44±0.02	5.26±0.87	Sa	1.0	Quiescent	2	No
RSCG51	NGC4274	400.58±1.28	220.32±0.74	297.65±0.93	395.81±2.29	SBab	1.7	Canyon	1	No
RSCG51	IC779	2.27±0.09	1.13±0.04	0.64±0.03	3.92±4.90	SABm	8.8	Canyon	2	Yes
RSCG51	NGC4314	253.73±3.10	135.89±1.39	133.08±0.07	278.67±0.49	Sa	1.0	Canyon	1	No
RSCG51	NGC4308	12.56±0.05	6.65±0.02	1.96±0.03	3.25±1.70	E	-4.8	Quiescent	2	Yes
RSCG52	MCG+07-25-060	8.63±0.11	4.62±0.06	4.04±0.04	3.83±1.15	E	-5.0	Quiescent	2	No
RSCG52	MCG+07-25-061	5.09±0.04	3.19±0.04	22.68±0.12	32.26±1.38	Sbc	4.3	Active	2	No
RSCG52	FIRSTJ122102.8+395205	5.83±0.03	3.82±0.01	31.58±0.03	61.04±1.68	Sc	4.8	Active	2	No
RSCG53	UGC7436	5.48±0.07	2.82±0.04	1.34±0.17	2.93±3.25	S0	-2.2	Quiescent	2	Yes
RSCG53	NGC4302	225.40±1.87	135.25±1.01	345.48±0.34	417.83±0.48	Sc	5.4	Active	1	No
RSCG53	NGC4298	120.77±1.11	71.29±0.64	312.71±0.56	456.26±2.52	Sc	5.2	Active	1	No
RSCG54	M85	912.16±6.31	483.91±3.39	136.59±0.64	23.16±1.35	S0-a	-1.3	Quiescent	2	No
RSCG54	NGC4394	158.20±1.45	84.58±0.59	107.20±0.58	18.30±1.24	SBb	3.0	Quiescent	2	No
RSCG55	MCG+02-32-054	4.30±0.07	2.51±0.03	10.33±0.06	61.24±1.81	Sa	0.5	Active	2	No
RSCG55	IC790	12.12±0.10	6.41±0.03	4.96±0.10	2.98±0.92	Sab	2.0	Quiescent	2	No
RSCG55	NGC4410F	0.47±0.01	0.27±0.01	1.36±0.04	3.24±1.28	-	-	Active	2	No
RSCG55	NGC4410NED01	5.72±0.50	3.37±0.27	4.82±0.18	16.45±1.21	Sab	1.7	Active	2	No
RSCG55	NGC4410NED02	2.66±0.25	1.40±0.14	0.58±0.15	3.27±0.95	Sa	0.5	Quiescent	2	No
RSCG56	NGC4440	70.54±0.26	36.28±0.15	13.05±0.05	4.20±1.10	Sa	1.1	Quiescent	2	No
RSCG56	NGC4436	10.29±0.19	5.47±0.08	1.85±0.02	3.16±4.48	S0	-1.8	Quiescent	2	Yes
RSCG57	NGC4451	33.82±0.22	20.06±0.07	93.86±0.24	139.53±0.29	Sab	2.4	Active	1	No
RSCG57	NGC4445	35.73±0.15	20.07±0.07	34.32±0.15	17.19±1.11	Sab	2.1	Quiescent	2	No
RSCG57	NGC4424	72.13±0.53	42.34±0.39	124.76±0.20	282.43±0.33	SBa	1.0	Active	1	No
RSCG57	NGC4417	145.14±0.86	76.34±0.39	24.32±0.09	8.40±0.90	S0	-1.9	Quiescent	2	No
RSCG57	NGC4442	340.49±0.89	177.69±0.47	54.65±0.41	14.53±1.22	S0	-1.9	Quiescent	2	No
RSCG57	IC3412	0.41±0.02	0.24±0.01	0.83±0.03	2.74±0.91	Sm	8.9	Active	2	No
RSCG58	NGC4458	37.40±0.37	19.60±0.14	6.18±0.29	4.14±1.06	E	-4.8	Quiescent	2	No
RSCG58	NGC4435	203.99±1.62	109.40±0.86	70.77±0.28	104.82±2.62	S0	-2.0	Quiescent	2	No
RSCG59	NGC4459	259.27±3.07	138.03±1.69	99.75±0.44	93.87±2.88	S0-a	-1.4	Quiescent	2	No
RSCG59	NGC4468	15.70±0.22	8.18±0.11	2.47±0.09	2.23±11.08	E-S0	-2.7	Quiescent	2	Yes
RSCG59	NGC4474	82.77±0.66	43.86±0.29	15.39±0.17	4.44±1.05	S0	-1.9	Quiescent	2	No
RSCG60	NGC4483	48.02±0.29	25.04±0.15	7.96±0.05	3.09±0.86	S0-a	-1.3	Quiescent	2	No
RSCG60	NGC4469	157.98±0.58	86.04±0.27	66.25±0.12	60.63±1.88	S0-a	0.3	Quiescent	2	No
RSCG60	UGC7590	2.31±0.11	1.35±0.05	3.76±0.12	15.52±1.05	Sc	5.1	Active	2	No
RSCG61	UGC7658	60.65±0.23	31.66±0.13	9.65±0.04	5.47±0.95	E	-5.0	Quiescent	2	No
RSCG61	NGC4486	1092.32±10.11	581.93±5.63	205.07±1.22	175.39±2.21	E	-4.3	Quiescent	1	No
RSCG61	NGC4478	128.96±0.37	67.23±0.16	19.86±0.12	6.74±1.37	E	-4.8	Quiescent	2	No
RSCG61	UGCA283	21.75±0.14	11.22±0.07	3.42±0.01	3.64±1.09	E	-5.0	Quiescent	2	No
RSCG61	NGC4476	39.91±0.30	21.92±0.14	28.71±0.11	30.15±1.44	E-S0	-3.0	Quiescent	2	No
RSCG62	NGC4491	28.96±0.24	16.81±0.12	44.93±0.21	277.18±6.03	SBa	1.2	Active	2	No
RSCG62	IC3446	1.86±0.02	1.06±0.01	1.82±0.04	3.87±1.07	Sm	9.4	Active	2	No
RSCG62	NGC4497	31.62±0.42	16.65±0.17	6.26±0.12	4.00±2.64	S0-a	-1.1	Quiescent	2	Yes
RSCG62	IC3461	1.69±0.04	0.88±0.03	0.18±0.01	3.61±3.28	E	-5.0	Quiescent	2	Yes
RSCG63	NGC4551	73.87±0.31	38.64±0.16	12.33±0.19	6.57±1.07	E	-4.9	Quiescent	2	No
RSCG63	M89	555.01±3.91	288.82±1.85	88.83±0.23	26.60±1.32	E	-4.6	Quiescent	2	No
RSCG63	IC3540	5.94±0.05	3.17±0.03	2.07±0.07	2.40±0.92	S0	-2.2	Quiescent	2	No
RSCG63	NGC4550	82.24±0.37	43.84±0.21	15.72±0.35	9.09±1.42	S0	-2.1	Quiescent	2	No
RSCG64	NGC4614	18.52±0.13	11.82±0.08	11.48±0.07	20.88±1.09	S0-a	0.0	Canyon	2	No
RSCG64	NGC4615	15.95±0.23	9.95±0.13	56.77±0.23	108.80±0.57	Sc	5.9	Active	1	No
RSCG64	NGC4613	5.17±0.04	2.88±0.03	9.03±0.06	23.89±1.42	Sc	4.8	Active	2	No
RSCG65	M60	1154.00±11.82	591.54±6.11	169.54±0.62	71.96±1.17	E	-4.6	Quiescent	1	No
RSCG65	NGC4647	145.40±5.75	86.70±3.12	408.98±4.57	623.74±2.47	SABc	5.2	Active	1	No
RSCG65	M59	436.02±3.58	227.27±2.01	67.97±0.11	21.30±1.22	E	-4.8	Quiescent	2	No
RSCG65	NGC4638	140.53±0.62	73.18±0.31	23.29±0.27	10.82±1.28	E-S0	-2.7	Quiescent	2	No
RSCG65	IC3653	13.97±0.05	7.22±0.03	2.25±0.10	3.70±2.05	E	-5.0	Quiescent	2	Yes
RSCG65	IC3652	4.00±0.09	2.10±0.04	0.60±0.04	2.41±12.00	E	-4.9	Quiescent	2	Yes
RSCG66	NGC4654	264.17±2.18	164.83±1.27	905.77±1.62	1608.18±2.48	Sc	5.9	Active	1	No
RSCG66	NGC4639	86.63±0.41	48.75±0.21	90.69±0.59	23.03±1.49	Sbc	3.5	Quiescent	2	No
RSCG69	IC870	12.14±0.06	7.78±0.04	51.80±0.17	96.43±0.43	Sc	5.5	Active	1	No
RSCG69	IC868	11.11±0.11	5.70±0.05	1.95±0.19	3.12±4.33	E	-5.0	Quiescent	2	Yes

Table 1—Continued

Group	Galaxy	W1 mJy	W2 mJy	W3 mJy	W4 mJy	Morphology	De Vaucouleurs number*	WISE Class**	Photometry type***	Upper Limit****
RSCG69	IC867	6.84±0.15	3.85±0.08	15.04±0.16	39.28±1.96	Sc	5.2	Active	2	No
RSCG70	NGC5143	1.13±0.02	0.68±0.01	2.90±0.01	4.79±0.80	SBd	7.8	Active	2	No
RSCG70	NGC5142	20.35±0.12	10.76±0.08	3.94±0.05	2.76±0.64	S0	-1.9	Quiescent	2	No
RSCG70	NGC5141	34.65±0.22	18.85±0.12	8.41±0.07	10.96±0.71	S0	-2.1	Quiescent	2	No
RSCG72	IC962	22.61±0.14	13.02±0.11	34.29±0.13	47.12±1.78	E?	0.0	Active	2	No
RSCG72	LEDA49627	12.89±0.09	7.77±0.06	32.48±0.16	36.61±1.39	Sab	2.1	Active	2	No
RSCG72	MCG+02-36-004	2.15±0.03	1.24±0.02	4.16±0.07	4.17±0.99	Sb	2.7	Active	2	No
RSCG73	MCG+02-36-018	3.70±0.06	2.11±0.03	4.07±0.02	20.01±0.92	Sbc	3.9	Active	2	No
RSCG73	NGC5423	24.38±0.24	12.75±0.13	4.32±0.01	1.77±0.75	E-S0	-3.0	Quiescent	2	No
RSCG73	MCG+02-36-016	7.29±0.04	3.86±0.02	2.98±0.08	5.23±1.11	Sb	2.7	Quiescent	2	No
RSCG74	NGC5504	21.85±0.09	13.64±0.06	74.62±0.12	150.83±0.12	Sbc	4.1	Active	1	No
RSCG74	IC4383	5.45±0.05	3.31±0.02	15.39±0.04	22.95±1.08	Sd	8.1	Active	2	No
RSCG74	UGC9086	0.48±0.03	0.27±0.01	0.76±0.02	2.49±1.07	Sd	8.1	Active	2	No
RSCG75	UGC9521	19.00±0.13	10.31±0.08	21.45±0.05	8.64±0.92	SBa	1.0	Quiescent	2	No
RSCG75	UGC9523	16.60±0.15	8.64±0.07	2.89±0.03	3.30±0.76	S0-a	-0.1	Quiescent	2	No
RSCG75	2MASXJ14471122+1135083	5.95±0.08	3.06±0.05	1.21±0.03	1.85±0.75	-	-	Quiescent	2	No
RSCG76	NGC5852	23.11±0.12	12.63±0.08	10.94±0.20	14.35±0.97	S0-a	-1.0	Quiescent	2	No
RSCG76	NGC5851	12.06±0.13	6.89±0.06	24.58±0.03	28.89±1.30	Sc	5.0	Active	2	No
RSCG76	MCG+02-38-043	5.52±0.02	3.49±0.02	18.61±0.02	21.42±1.32	Sab	1.5	Active	2	No
RSCG78	NGC6964	27.60±0.48	14.50±0.29	4.39±0.18	3.02±1.23	E	-4.5	Quiescent	2	No
RSCG78	NGC6962	52.53±1.19	27.81±0.73	17.43±1.26	6.54±1.32	SABa	1.7	Quiescent	2	No
RSCG78	NGC6961	9.38±0.05	5.46±0.02	5.74±0.09	10.47±1.32	E	-4.1	Canyon	2	No
RSCG78	NGC6959	12.42±0.10	6.64±0.07	2.91±0.04	3.57±1.28	S0	-1.8	Quiescent	2	No
RSCG79	MCG-04-50-007	9.23±0.25	4.90±0.16	1.58±0.13	6.47±6.05	S0	-2.0	Quiescent	2	Yes
RSCG79	MCG-04-50-006	3.31±0.08	1.79±0.04	0.63±0.10	10.86±20.25	S0-a	-1.0	Canyon	2	Yes
RSCG83	NGC7465	51.07±0.14	34.50±0.14	145.12±0.55	330.28±2.48	S0	-1.8	Active	1	No
RSCG83	NGC7464	1.55±0.06	0.88±0.04	2.06±0.17	13.52±1.31	E	-4.9	Active	2	No
RSCG83	NGC7463	24.50±0.13	15.32±0.05	86.68±0.15	164.74±0.45	SABb	3.1	Active	1	No
RSCG84	NGC7534	2.84±0.04	1.66±0.02	5.45±0.11	10.86±1.29	IB	9.9	Active	2	No
RSCG84	NGC7532	11.16±0.05	7.26±0.04	45.75±0.17	175.99±4.55	S0-a	-0.7	Active	2	No
RSCG84	NGC7530	4.31±0.03	2.58±0.02	11.24±0.02	35.91±1.50	S0-a	0.0	Active	2	No
RSCG85	UGC12545	3.59±0.04	2.08±0.04	6.87±0.11	8.28±1.12	SBc	5.9	Active	2	No
RSCG85	UGC12546	7.41±0.04	4.42±0.03	20.64±0.13	17.34±1.07	Sbc	4.0	Active	2	No
RSCG85	UGC12543	1.89±0.07	1.11±0.03	3.55±0.04	4.66±0.98	Sc	5.8	Active	2	No
RSCG86	IC5342	6.22±0.08	3.16±0.04	1.03±0.02	3.15±5.13	E	-4.9	Quiescent	2	Yes
RSCG86	2MASXJ23383626+2701467	4.59±0.09	2.35±0.05	1.07±0.05	4.37±1.10	S0	-2.5	Quiescent	2	No
RSCG86	NGC7720	20.61±0.44	10.56±0.21	3.99±0.16	5.69±0.91	E	-4.3	Quiescent	3	No
RSCG88	IC5353	17.81±0.21	9.31±0.13	2.75±0.04	3.52±2.39	E-S0	-3.2	Quiescent	2	Yes
RSCG88	IC5354	8.02±0.13	4.33±0.07	2.26±0.03	2.89±0.90	E	-4.3	Quiescent	2	No

Note. — *The morphological types and De Vaucouleurs numbers are from the HyperLeda database (Paturel et al. 2003a,b), which accumulates morphologies from available publications and compares and combines them to determine an optimal De Vaucouleurs number and classification for each galaxy. **See §3.2 and Figure 2 for explanation of WISE classification scheme [Quiescent, Canyon, Active]. ***See §2.2 for description of photometry types. ****This column indicates whether there is an upper limit in a single band (either W3 or W4); galaxies with upper limits in more than one band are excluded from the full sample. In cases where the galaxy has an upper limit, the error in that band is set to null in the ALLWISE source catalog, and we quote the ratio of $\frac{S}{SNR}$ as the uncertainty.